

VLT/GIRAFFE spectroscopic observations of the metal-poor blue compact dwarf galaxy SBS 0335–052E^{***}

Y. I. Izotov¹, D. Schaerer^{2,3}, A. Blecha², F. Royer⁴, N. G. Guseva¹, and P. North⁵

¹ Main Astronomical Observatory, Ukrainian National Academy of Sciences, Zabolotnoho 27, Kyiv 03680, Ukraine

² Observatoire de Genève, 51, Ch. des Maillettes, 1290 Sauverny, Switzerland

³ Laboratoire d'Astrophysique Toulouse-Tarbes, UMR 5572, 14, Av. E. Belin, 31400 Toulouse, France

⁴ GEPI, CNRS UMR 8111, Observatoire de Paris, 5 place Janssen, 92195 Meudon Cedex, France

⁵ Laboratoire d'Astrophysique, École Polytechnique Fédérale de Lausanne (EPFL), Observatoire, 1290 Sauverny, Switzerland

Received ; Accepted

ABSTRACT

Aims. We present two-dimensional spectroscopy of the extremely metal-deficient blue compact dwarf (BCD) galaxy SBS 0335–052E aiming to study physical conditions, element abundances and kinematical properties of the ionised gas in this galaxy.

Methods. Observations were obtained in the spectral range $\lambda 3620 - 9400\text{\AA}$ with the imaging spectrograph GIRAFFE installed on the UT2 of the Very Large Telescope (VLT). These observations are the first ones carried out so far with GIRAFFE in the ARGUS mode which allows to obtain simultaneously 308 spectra covering a $11''.4 \times 7''.3$ region.

Results. We produced images of SBS 0335–052E in the continuum and in emission lines of different stages of excitation. We find that while the maximum of emission in the majority of lines, including the strong lines H β 4861 \AA , H α 6563 \AA , [O III] 4363,5007 \AA , [O II] 3726,3729 \AA , coincides with the youngest south-eastern star clusters 1 and 2, the emission of He II 4686 \AA line is offset to the more evolved north-west clusters 4, 5. This suggests that hard ionising radiation responsible for the He II $\lambda 4686\text{\AA}$ emission is not related to the most massive youngest stars, but rather is connected with fast radiative shocks. This conclusion is supported by the kinematical properties of the ionised gas from the different emission lines as the velocity dispersion in the He II $\lambda 4686\text{\AA}$ line is systematically higher, by $\sim 50\% - 100\%$, than that in other lines. The variations of the emission line profiles suggest the presence of an ionised gas outflow in the direction perpendicular to the galaxy disk. We find a relatively high electron number density N_e of several hundred cm^{-3} in the brightest part of SBS 0335–052E. There is a small gradient of the electron temperature T_e and oxygen abundance from the East to the West with systematically higher T_e and lower $12 + \log \text{O}/\text{H}$ in the western part of the galaxy. The oxygen abundances for the whole H II region and its brightest part are $12 + \log \text{O}/\text{H} = 7.29 \pm 0.02$ and 7.31 ± 0.01 , respectively. We derive the He mass fraction taking into account all systematic effects. The He mass fraction $Y = 0.2463 \pm 0.0030$, derived from the emission of the whole H II region, is consistent with the primordial value predicted by the standard big bang nucleosynthesis model. We confirm the presence of Wolf-Rayet stars in the cluster 3.

Key words. galaxies: fundamental parameters – galaxies: starburst – galaxies: ISM – galaxies: abundances – galaxies: individual (SBS 0335–052E)

1. Introduction

The blue compact dwarf (BCD) galaxy SBS 0335–052E is an excellent nearby laboratory for studying star formation in low-metallicity environments. Since its discovery as one of the most metal-deficient star-forming galaxies known (Izotov et al. , 1990), with oxygen abun-

dance $12 + \log \text{O}/\text{H} \sim 7.30$ (Melnick et al. , 1992; Izotov et al. , 1997b, 1999; Thuan & Izotov , 2005), SBS 0335–052E has often been proposed as a nearby young dwarf galaxy (Izotov et al. , 1990, 1997b; Thuan et al. , 1997; Papaderos et al. , 1998; Pustilnik et al. , 2004). Thuan et al. (1997) and Papaderos et al. (1998), using the same Hubble Space Telescope (HST) images, have found several luminous clusters. The brightest clusters are labelled in Fig. 1 which represents the highest spatial resolution archival UV HST/Advanced Camera for Surveys (ACS) image of SBS 0335–052E

Send offprint requests to: Y. I. Izotov, izotov@mao.kiev.ua

* Based on VLT observations collected at the European Southern Observatory, Chile, Swiss GTO program 072.B-0237.

** Tables 4 and 5 are available only in the electronic version of the paper.

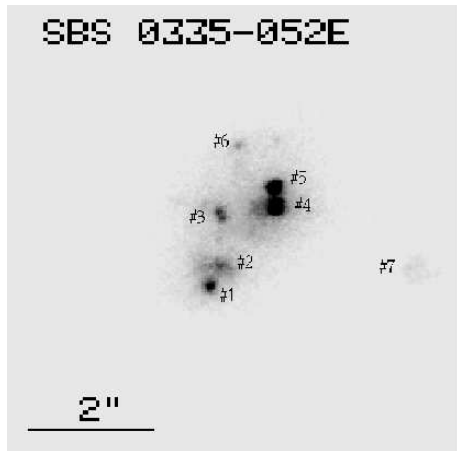


Fig. 1. Archival HST/ACS UV image of SBS 0335–052E with the labelled compact clusters. North is up and East is to the left.

obtained by Kunth et al. (2003). Some of the clusters are very young and produce extended regions of ionised gas (Melnick et al. , 1992; Izotov et al. , 1997b; Papaderos et al. , 1998; Pustilnik et al. , 2004). In particular, Izotov et al. (2001b), using deep long-slit spectra of SBS 0335–052E, have shown that extended H α emission is detected over ~ 6 –8 kpc, suggesting that hot ionised gas is spread out far away from the central part of the galaxy.

Thuan & Izotov (1997) using HST/GHRS UV spectrum of SBS 0335–052E have discovered a very broad Ly α line in absorption suggesting that this galaxy is embedded in a large envelope of neutral gas. The column density of $N(\text{H I}) = 7 \times 10^{21} \text{ cm}^{-2}$ in SBS 0335–052E derived by Thuan & Izotov (1997) is the largest one known for the BCDs. Later, Pustilnik et al. (2001) using Very Large Array (VLA) observations in the line H I $\lambda 21$ cm have detected a large neutral gas cloud around SBS 0335–052E with a size 66 by 22 kpc elongated in the east-west direction and with two maxima separated by 22 kpc. The first maximum in H I distribution is connected to SBS 0335–052E, and the second one to the companion dwarf galaxy SBS 0335–052W discovered by Pustilnik et al. (1997). The latter galaxy is shown by Izotov et al. (2005) to be the lowest metallicity emission-line galaxy known with $12 + \log \text{O/H} = 7.12 \pm 0.03$. Thuan et al. (2005) using Far Ultraviolet Spectroscopic Explorer (FUSE) observations have found that the oxygen abundance of the neutral gas around SBS 0335–052E of $12 + \log \text{O/H} \sim 7.0$ is only slightly lower than that of the ionised gas, implying that this galaxy was not formed from pristine gas.

Despite the low metallicity of SBS 0335–052E, an appreciable amount of dust has been detected in it. Izotov et al. (1997b) and Thuan et al. (1997) have found variations of extinction in this galaxy from the optical spectroscopic and photometric observations. Later, Thuan et al. (1999) and Houck et al. (2004) using Infrared Space Observatory (ISO) and Spitzer mid-infrared observations have found an emission of an appre-

ciable amount of warm dust with a characteristic temperature of ~ 100 K. Even hotter dust with a temperature of several hundred degrees is expected to be present in SBS 0335–052E which is indicated in the infrared spectra at shorter wavelengths, namely 2–4 μm (Vanzi et al. , 2000; Hunt et al. , 2001).

Since the discovery paper by Izotov et al. (1990) it is known that the ionising radiation in SBS 0335–052E is hard. The presence of the high-ionisation He II $\lambda 4686 \text{ \AA}$ emission line (e.g. Izotov et al. , 1990; Melnick et al. , 1992; Izotov et al. , 1997b) and of the [Fe V] $\lambda 4227 \text{ \AA}$ emission line (Izotov et al. , 2001b; Fricke et al. , 2001) suggests that radiation with photon energies greater than 4 Rydberg is intense and could not be explained by stellar emission. Furthermore, Izotov et al. (2001b) and Thuan & Izotov (2005) have found [Fe VII] and [Ne V] emission lines which require intense radiation with photon energies above 7 Rydberg. SBS 0335–052E has also been detected in the X-ray range (Thuan et al. , 2004). The origin of the hard ionising radiation remains unclear. Several mechanisms such as radiation from most massive main-sequence stars, Wolf-Rayet stars, high-mass X-ray binaries and radiative shocks have been discussed by e.g. Garnett et al. (1991), Schaerer (1996), Izotov et al. (2001b), Izotov et al. (2004) and Thuan & Izotov (2005). The most recent investigations have shown that although the stellar origin of hard radiation is not completely excluded, the most likely source of hard radiation is fast radiative shocks.

Despite the efforts of different groups in studying the properties of SBS 0335–052E and its evolutionary status many problems remain unsolved. Since this galaxy is possibly a young galaxy it could be considered as a local counterpart of the high-redshift young dwarf galaxies. Therefore the continuation of its studies is important for cosmological applications. In this paper we present a two-dimensional spectroscopic study of SBS 0335–052E with the VLT/GIRAFFE. These are the first observations carried out so far in the ARGUS mode. Two new features are characteristic for these new observations which were not present in all previous spectroscopic studies of this galaxy. First, new observations allow to map the whole galaxy in different emission lines and in the continuum. This gives integrated characteristics of different emission lines for the whole H II region, such as the line luminosities, which are necessary input parameters for building up the model of the H II region. Second, the spectral resolution of new observations is by one order of magnitude better than in all previous spectroscopic observations of SBS 0335–052E and it is enough to obtain the intrinsic profiles of emission lines. This allows to study the kinematics of the H II region, and to make a comparison of kinematic characteristics in regions of different ionisation stages. In particular, it is important to compare the He II $\lambda 4686 \text{ \AA}$ line profiles with the profiles of other emission lines and, hence, to make conclusions concerning the origin of hard radiation in SBS 0335–052E.

Table 1. Journal of observations

Date	Setup	Wavelength range, Å	Resolving power R	Exposure, s	Airmass ^a	Seeing ^a
19 Nov 2003	LR1	3620–4081	12800	2×1200	1.066, 1.065	1''.3, 0''.9
20 Nov 2003	LR2	3964–4567	10200	2×1200	1.082, 1.062	0.8, 0.8
20 Nov 2003	LR3	4501–5078	12000	2×1350	1.061, 1.080	1.0, 0.7
21 Nov 2003	LR4	5010–5831	9600	2×1200	1.295, 1.170	0.8, 0.8
21 Nov 2003	LR5	5741–6524	11800	2×1500	1.070, 1.066	1.3, 0.7
21 Nov 2003	LR6	6438–7184	13700	2×1200	1.067, 1.103	1.0, 0.7
21 Nov 2003	LR7	7102–8343	8900	2×1200	1.286, 1.486	0.8, 0.9
22 Nov 2003	LR8	8206–9400	10400	2×1200	1.076, 1.061	0.7, 0.8

^aThe first value is at start of exposure, the second value is at end of exposure.

In §2 we describe the observations and data reduction. Morphology of SBS 0335–052E in different emission lines and continuum is considered in §3. Kinematic properties are discussed in §4. Heavy element abundances and helium abundance are derived in §5. The Wolf-Rayet stellar population in SBS 0335–052E is discussed in §6. Our conclusions are summarised in §7.

2. Observations and Data Reduction

Observations of SBS 0335–052E with the VLT/GIRAFFE spectrograph have been done during the nights 19 – 22 November, 2003 in the entire visible range. GIRAFFE is equipped with a 2K×4K EEV CCD. The size of the CCD pixels is 15 μm ×15 μm . The spatial scale is 0''.52/pixel in ARGUS direct mode which was used during our observations. The ARGUS array is a rectangular array of 22 by 14 microlenses which is fixed at the center of one positioner arm. We used a spatial scale with a sampling of 0''.52 per microlens and a total aperture of 11''.4×7''.3. The major axis of the array was directed along the major axis of SBS 0335–052E at a position angle P.A. = -30° and centered on the cluster 1 (Fig. 1). The low-resolution mode with the 600 lines/mm grating has been used. Since the wavelength coverage with this grating ranges from 400Å to 1200Å depending on the central wavelength, eight exposures have been done with setups LR1 – LR8 (Table 1) to obtain panoramic spectra in the wavelength range 3620 – 9400Å and a spectral resolution of 0.5 – 1Å. Each exposure was split in two subexposures for removal of cosmic ray hits. The journal of observations is shown in Table 1. Additionally, for the same setups the spectra of two standard stars, Feige 110 and HD 49798, have been obtained for flux calibration. During the days the exposures of bias, Nasmyth screen flats and comparison lamps for the wavelength calibration have been obtained. The description of GIRAFFE may be found in Pasquini et al. (2002).

The spectra were extracted and calibrated using the standard *Python* version of BLDRS - Baseline Data Reduction Software (girbldrs-1.12) available from <http://girbldrs.sourceforge.net>. Basic description of BLDRS is given in Blecha et al. (2000) and Royer et al. (2002). The processing includes the bias subtraction, correction for the pixel sensitivity variations, localisation,

optimal extraction, rebinning to linear wavelength scale and night sky subtraction.

The flux calibration has been done using IRAF¹. The flux-calibrated and redshift-corrected spectrum of the brightest rectangular region delineated by the thick solid line in the center of Fig. 7a is shown in Fig. 2. The region includes clusters 1 and 2. Many strong permitted and forbidden emission lines are seen in the spectrum of this region. One important feature of this spectrum is that its spectral resolution is the highest among all other spectra of SBS 0335–052E obtained so far. In particular, several blends are resolved for the first time for this object, most notably, [O II] λ 3726 and [O II] λ 3729, He I λ 3965, [Ne III] λ 3967 and H7 λ 3970, [Ar IV] λ 4711 and He I λ 4713. The spectrum contains emission lines of ions of a broad range of ionisation stages. In particular, [Fe II], [Fe III], [Fe IV], [Fe V], [Fe VI] and [Fe VII] emission lines are detected.

The spectrum of another region centered on the clusters 4 and 5 and delineated by the thick dashed line in Fig. 7a is shown in Fig. 3. The level of continuum in this spectrum is comparable to that in the spectrum of the brightest region (Fig. 2), but emission lines are weaker.

The emission line fluxes and widths were measured in each of the 22×14 lens array using the routine SPLOT in IRAF. Flux errors were derived from the photon statistics using non-flux-calibrated spectra. These errors were propagated in the determination of the electron temperatures, electron number densities and element abundances.

3. Morphology in Continuum and Emission Lines

One of the advantages of the SBS 0335–052E panoramic observations with GIRAFFE/ARGUS is that the spectra of each region with an angular size of 0''.52×0''.52 within an aperture 11''.4×7''.3 were obtained. This allows us to study the morphology of the galaxy in the continuum and individual emission lines and to construct the model of its H II region.

¹ IRAF is the Image Reduction and Analysis Facility distributed by the National Optical Astronomy Observatory, which is operated by the Association of Universities for Research in Astronomy (AURA) under cooperative agreement with the National Science Foundation (NSF).

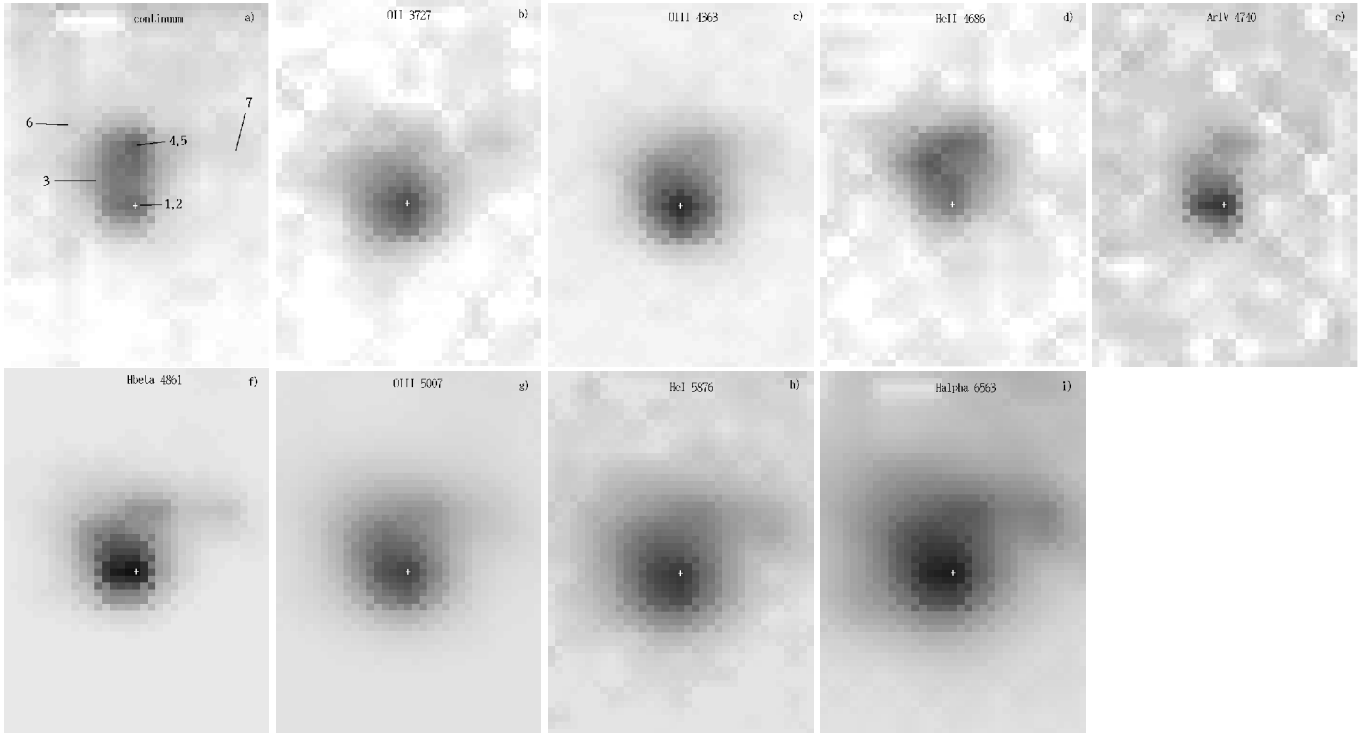


Fig. 4. Images in the continuum near $H\beta$ emission line (a) and in emission lines $[O\ II]\ \lambda 3727\text{\AA}$ (b), $[O\ III]\ \lambda 4363\text{\AA}$ (c), $He\ II\ \lambda 4686\text{\AA}$ (d), $[Ar\ IV]\ \lambda 4740\text{\AA}$ (e), $H\beta\ \lambda 4861\text{\AA}$ (f), $[O\ III]\ \lambda 5007\text{\AA}$ (g), $He\ I\ \lambda 5876\text{\AA}$ (h) and $H\alpha\ \lambda 6563\text{\AA}$ (i). All images are shown in the logarithmic flux scale. Positions of stellar clusters are labelled in panel (a). White cross in each panel shows the location of the region with maximum flux of the $H\alpha\ \lambda 6563\text{\AA}$ emission line.

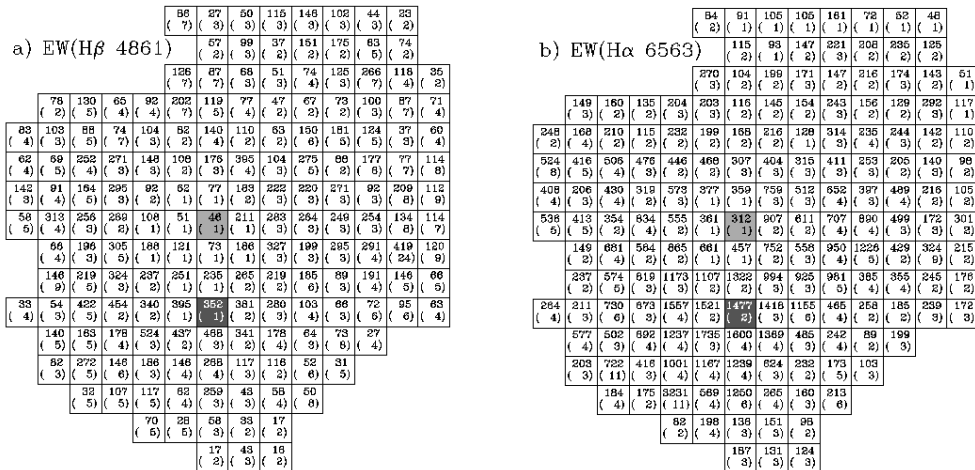


Fig. 5. Distribution of the $H\beta\ \lambda 4861\text{\AA}$ equivalent width (a) and of the $H\alpha\ \lambda 6563\text{\AA}$ equivalent width (b) in \AA , with errors indicated in parentheses. Each square region corresponds to $0''.52 \times 0''.52$. Only regions in which both $EW(H\beta)$ and $EW(H\alpha)$ could be measured are shown. Dark squares indicate the locations of clusters 1+2 with the maximum flux of the $H\alpha$ emission line, grey squares the locations of clusters 4+5.

The central part of SBS 0335–052E containing the brightest clusters has an angular size $\lesssim 2''$ (Fig. 1) which is only $\lesssim 4$ times larger than the angular size of $0''.52$ of each ARGUS lens. Therefore, for better viewing we rebinned the images, splitting each pixel in 9 from $0''.52$ pixel sizes to $0''.17$ pixel sizes linearly interpolating flux values in adjacent $0''.52$ pixels. In Fig. 4 are shown the rebinned images of SBS 0335–052E in the continuum near $H\beta\ \lambda 4861\text{\AA}$ (a),

and in the emission lines $[O\ II]\ \lambda 3727\text{\AA}$ (b), $[O\ III]\ \lambda 4363\text{\AA}$ (c), $He\ II\ \lambda 4686\text{\AA}$ (d), $[Ar\ IV]\ \lambda 4740\text{\AA}$ (e), $H\beta\ \lambda 4861\text{\AA}$ (f), $[O\ III]\ \lambda 5007\text{\AA}$ (g), $He\ I\ \lambda 5876\text{\AA}$ (h) and $H\alpha\ \lambda 6563\text{\AA}$ (i). In all panels white crosses denote the pixel with the largest flux of the $H\alpha\ \lambda 6563\text{\AA}$ emission line which is coincident with the location of clusters 1+2 in Fig. 1.

The image in the continuum (Fig. 4a) with labelled clusters resembles well the HST UV image (Fig. 1) despite

the much lower angular resolution determined by a seeing of $\sim 1''$ (Table 1). Several clusters are seen. However, the angular resolution in the GIRAFFE data is not enough to separate clusters 1 and 2, and 4 and 5.

The images in all emission lines (except for the He II $\lambda 4686\text{\AA}$ line) are very similar. They show very bright emission in the region of clusters 1, 2 and much fainter emission in the direction of other clusters. Furthermore, the equivalent widths of H β $\lambda 4861\text{\AA}$ and H α $\lambda 6563\text{\AA}$ emission lines in the clusters 1 and 2 (dark squares in Fig. 5) and in the regions around these clusters are high. These facts suggest that clusters 1 and 2 are young, with an age 3–4 Myr, and contain numerous hot and massive ionising main-sequence stars. It is likely, that clusters 7 and probably 3 are also young because EW(H β) and EW(H α) are high. However, the number of ionising massive stars in those clusters is much lower than in clusters 1 and 2. On the other hand, clusters 4, 5 and 6 are probably more evolved as evidenced by their lower equivalent widths of H β $\lambda 4861\text{\AA}$ and H α $\lambda 6563\text{\AA}$ emission lines. In particular, the H β equivalent width EW(H β) = 46\AA for clusters 4, 5 (grey square in Fig. 5) and 87\AA for the square region delineated by the thick dashed line correspond to an age of $\sim 6 - 8$ Myr and ~ 5 Myr adopting heavy element mass fraction $Z = 0.001$ for stars (Schaerer & Vacca, 1998). Age for clusters 4,5 is larger if lower $Z = 0.0004$ corresponding to the metallicity of the ionised gas is adopted. The larger age of clusters 4 and 5 is supported by their weak P α emission as compared to that of clusters 1 and 2 (Thompson et al., 2006). The different age of clusters 1+2 and 4+5 could in principle explain why the brightness of clusters 4 and 5 in the UV range is greater than that of clusters 1 and 2 (Fig. 1), why their brightness is comparable in the optical continuum (Fig. 4a) and why clusters 4 and 5 are fainter in the NIR (Thompson et al., 2006). This is because the relative contribution of the ionised gas emission is increased from the UV to the NIR. The effect is stronger for clusters 1 and 2 because of the higher EW(H β) and hence of higher contribution of the ionised gas to the total emission. In addition, the interstellar extinction may play role if it is higher for clusters 1 and 2.

The morphology of SBS 0335–052E in the He II $\lambda 4686\text{\AA}$ emission line (Fig. 4d) significantly differs from that in other emission lines. The emission of this line in the direction of the clusters 3 and 4+5 is stronger than that in the direction of the clusters 1 and 2. This offset of the He II $\lambda 4686\text{\AA}$ emission line relative to other nebular lines was noted earlier by Izotov et al. (1997b) and Izotov et al. (2001b). Thus, it is evident that the hard ionising radiation responsible for the He II $\lambda 4686\text{\AA}$ emission is not connected with the young main-sequence stars, but rather related to the post-main-sequence stars or their remnants. This effect is more clearly seen in Fig. 6 where we show the distribution of the relative flux He II $\lambda 4686/\text{H}\beta$. In the direction on the clusters 1 and 2 the relative He II $\lambda 4686/\text{H}\beta$ flux is $\sim 1-2\%$ while in north-west regions it increases to $\sim 6 - 7\%$. Such high relative fluxes of the He II $\lambda 4686$ emission line is difficult to explain by the ionising stel-

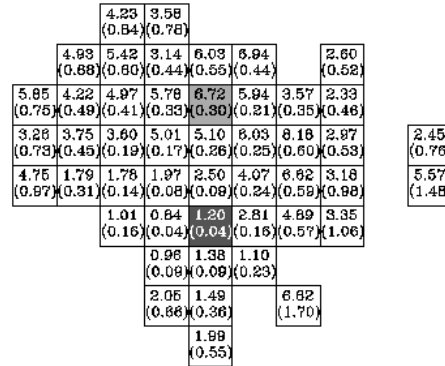


Fig. 6. He II $\lambda 4686/\text{H}\beta$ relative intensity distribution (in percent). Only regions with a strong enough He II $\lambda 4686$ emission line are shown. The dark square is the location of clusters 1+2, while the grey square is the location of clusters 4+5.

lar radiation (Izotov et al., 2004; Thuan & Izotov, 2005, e.g.). Although a small number of Wolf–Rayet stars are found in cluster 3 (see Papaderos et al., 2006, and this paper), other mechanisms such as radiative shocks need to be invoked.

4. Kinematics of the Ionised Gas

The second advantage of the present GIRAFFE spectra for SBS 0335–052E is that they are obtained with sufficient enough spectral resolution. Therefore, the panoramic spectroscopic data can be used to study the kinematics of the H II regions in this galaxy.

In Fig. 7 we show the profiles of the H α $\lambda 6563\text{\AA}$ (a), He II $\lambda 4686\text{\AA}$ (b), [O II] $\lambda 3726, 3729\text{\AA}$ (c) and [O III] $\lambda 4363\text{\AA}$ (d) emission lines in each pixel of the ARGUS array. Dotted lines show the wavelengths of emission lines adopting the average redshift derived from the observed wavelengths of all strong emission lines in the spectrum of the brightest rectangular region delineated by a thick solid line in Fig. 7a. H α $\lambda 6563\text{\AA}$ is the strongest line in all ARGUS array spectra and thus allows to study the kinematical properties in the low-intensity extended regions of SBS 0335–052E. Other lines originate in different zones of the H II region: He II $\lambda 4686\text{\AA}$ is a characteristic of the highest ionisation zone, [O II] $\lambda 3726, 3729\text{\AA}$ are characteristics of the lowest ionisation zone, and [O III] $\lambda 4363\text{\AA}$ emission corresponds to the intermediate zone which is overlapped with the highest- and lowest-ionisation zones.

H α emission is seen almost in the whole region observed with GIRAFFE (Fig. 7a). The total aperture $11''.4 \times 7''.3$ of ARGUS corresponds to linear size ~ 3.1 kpc \times 1.8 kpc adopting the distance to SBS 0335–052E of 54.3 Mpc (Izotov et al., 1997b). Thus, the observed region is only a part of a much larger H II region with a size of $\sim 6 - 8$ kpc detected by Izotov et al. (2001b). In the brightest central region and in the slice oriented west-east the H α $\lambda 6563$ line is narrow and no systematic offset of the line profile from the dotted line is seen. Thus, no

evidence is present for the rotation of the observed part of the galaxy, since the west-east orientation of the region with narrow profiles is close to that for the disk-like H I cloud seen edge-on (Pustilnik et al. , 2001). On the other hand, in the north-south direction the H α profiles are much broader and with more complex structure, suggesting an outflow of ionised gas in the direction perpendicular to the H I disk. The schematic H α kinematic model is shown in Fig. 8 where the grey rectangular region is the region with narrow H α profiles which is oriented approximately along the H I cloud detected by Pustilnik et al. (2001). Two regions with the ionised gas outflow are shown to the north and south of the region with the narrow H α line. The double-peaked H α profiles in the northern and southern parts of Fig. 7a suggest the presence of expanding shells of ionised hydrogen with radial components of velocities of $\sim 50 \text{ km s}^{-1}$. This finding is consistent with the presence of a shell of ionised gas at an angular distance of $\sim 5''$ to the north from the cluster 1 (Thuan et al. , 1997). The width of H α in clusters 4, 5 (grey square in Fig. 7a) is ~ 2 times larger than that in clusters 1 and 2 (dark square in Fig. 7a) implying higher dynamic activity of the interstellar medium in the former, older clusters. This higher activity is probably due to supernova explosions.

All observed profiles were fit with a single gaussian profile. In Fig. 9a we show FWHMs of the H α emission line in km s^{-1} due to the macroscopic motion only. Errors are given in parentheses. The widths are obtained after correction for the instrumental profiles and for the thermal motion, following the formula

$$\text{FWHM}_{tur}^2 = \text{FWHM}_{obs}^2 - \text{FWHM}_i^2 - \text{FWHM}_{th}^2, \quad (1)$$

where FWHM_{tur} , FWHM_{obs} , FWHM_i and FWHM_{th} are the width of the macroscopic motion, the observed width, the width of the instrumental profile and the width of the thermal motion, respectively. The FWHM_i is obtained from the profiles of night sky emission lines and it is $\sim 25 \text{ km s}^{-1}$. The width of the thermal profile of 30 km s^{-1} is derived for the electron temperature $T_e = 20000\text{K}$ and it is applied to the H α $\lambda 6563\text{\AA}$, He II $\lambda 4686\text{\AA}$ and [O III] $\lambda 4363\text{\AA}$ emission lines, while the width of 26 km s^{-1} is obtained for $T_e = 15000\text{K}$ and it is applied to the [O II] $\lambda 3729\text{\AA}$ emission line.

In the brightest part of SBS 0335–052E the $\text{FWHM}(\text{H}\alpha)$ in and around the clusters 1 and 2 is $\sim 40 \text{ km s}^{-1}$. This value is lower than the $\text{FWHM}(\text{H}\alpha)$ of 83 km s^{-1} and 62 km s^{-1} derived by Petrosian et al. (1997) for the NW and SE components of I Zw 18. Apparently, the dispersion of macroscopic motion is strongly dependent on the age of starburst and it is larger in the evolved starbursts where the SNe activity is higher. Indeed, the difference between clusters 1 and 2 in SBS 0335–052E and the NW and SE components of I Zw 18 is that the clusters 1 and 2 are younger as the equivalent width of the H β emission line there, $\text{EW}(\text{H}\beta) \sim 300 - 400\text{\AA}$ (Fig. 5a), is much larger than the $\text{EW}(\text{H}\beta) \lesssim 100\text{\AA}$ in the NW and SE

components of I Zw 18. It is probable that SNe have not yet appeared or their number is small in clusters 1 and 2.

On the other hand, the macroscopic motion in and around the older clusters 4 and 5 is significantly larger with $\text{FWHM}(\text{H}\alpha) \sim 100 \text{ km s}^{-1}$, likely due to a high SN activity. Similar FWHM values and a similar spatial behaviour are found for the [O II] $\lambda 3729\text{\AA}$ and [O III] $\lambda 4363\text{\AA}$ emission lines. (Figs. 9c and 9d). The tendency of higher FWHM in more evolved clusters is also retained for the He II $\lambda 4686\text{\AA}$ emission line (Fig. 9b). However, the macroscopic velocity in the regions of He II emission is significantly larger than that in the emission regions of other lines. This difference may be an additional indication that the source of hard radiation is connected with fast radiative shocks.

5. Physical Conditions and Element Abundances

The large aperture ($11''.4 \times 7''.3$), high enough spectral resolution and large wavelength coverage of the ARGUS observations allow the detailed study of physical conditions (electron temperature and electron number density) and element abundances in the H II region. However, there are some limitations to this study. First, observations in different wavelength ranges have been done not in single but in separate exposures during several nights (see Table 1). Therefore, due to the varying weather conditions (seeing, transparency), effects of the atmospheric refraction and non-perfect pointing during different exposures the spectra in small apertures such as in a single pixel of $0''.52 \times 0''.52$ and in different wavelength ranges are not quite well adjusted since they represent slightly different regions of the galaxy. These effects tend to be lower with increasing aperture. Therefore, depending on the adopted aperture, we will follow different approaches in the determination of element abundances. We consider the element abundance determination from the spectra obtained in apertures with three different sizes. First, for the spectra obtained within the largest available aperture of $11''.4 \times 7''.3$ there is no need to adjust the different wavelength ranges. This allows to correct consistently the spectra for interstellar extinction using the observed decrement of hydrogen Balmer lines and then derive element abundances. Second, we consider the spectrum of the brightest region of SBS 0335–052E obtained within an aperture $1''.56 \times 1''.04$ (the rectangular region delineated by a thick solid line in Fig. 7a). This spectrum is shown in Fig. 2. Since the aperture for this spectrum is relatively small, some adjustment of adjacent wavelength ranges is needed. However, thanks to the high brightness of this region many bright emission lines are seen in its spectrum. Therefore we use the same brightest emission lines in the overlapping wavelength ranges (where this is possible) to scale the spectra in the adjacent wavelength ranges. These lines are H7 $\lambda 3970\text{\AA}$, He I $\lambda 4471\text{\AA}$, [O III] $\lambda 4959\text{\AA}$, [O I] $\lambda 6300\text{\AA}$ and He I $\lambda 7065\text{\AA}$. In the remaining two overlapping wavelength ranges $\lambda 5650-5750$ and $\lambda 8100-8200$ where no strong emission lines are seen we used the continuum levels to adjust

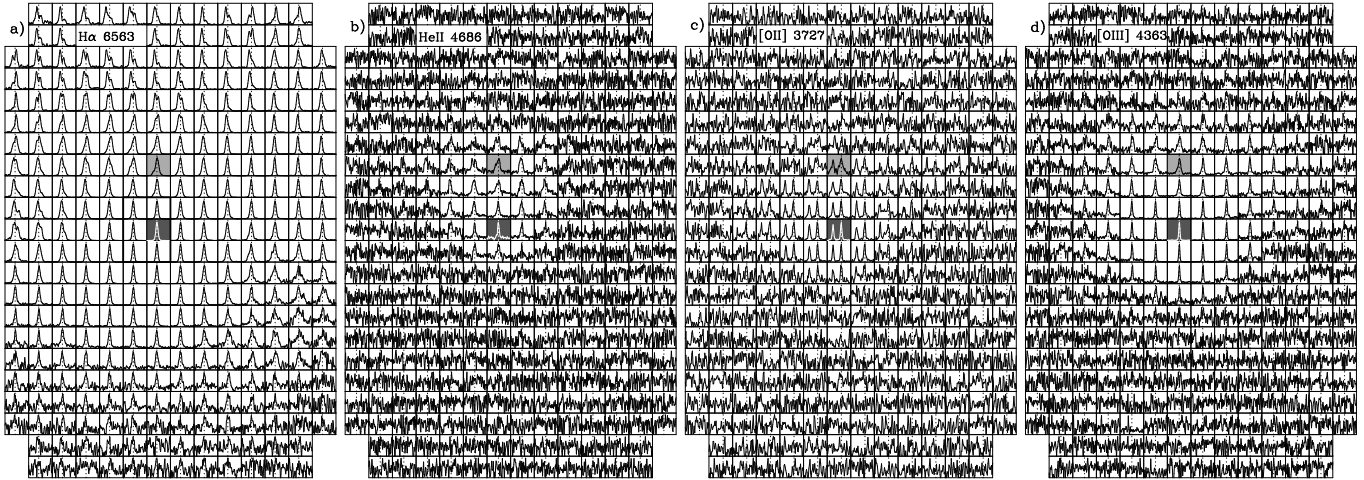


Fig. 7. Profiles of the emission lines: (a) $H\alpha$ $\lambda 6563\text{\AA}$, (b) $He\ II$ $\lambda 4686\text{\AA}$, (c) $[O\ II]$ $\lambda 3726, 3729\text{\AA}$ and (d) $[O\ III]$ $\lambda 4363\text{\AA}$. All $0''.52 \times 0''.52$ regions are shown. Dark squares mark the location of clusters 1+2, grey squares the location of clusters 4+5. Thick solid and thick dashed lines in (a) delineate respectively the brightest rectangular region and the second brightest square region for which the spectra are shown in Fig. 2 and 3.

the adjacent spectra. Thus, in the spectrum of the brightest region the determination of the interstellar extinction is still possible, which was used to correct the spectra. Third, in the case of smallest apertures of $0''.52 \times 0''.52$, in general the signal-to-noise of the spectra is not enough to use the same emission lines in the overlapping wavelength ranges. Therefore, for these apertures we adjust spectra in different wavelength ranges assuming that the ratios of hydrogen Balmer lines correspond to the theoretical values at the electron temperature of $T_e = 20000\text{K}$. Hence, no determination of the interstellar extinction is possible for the smallest apertures and not all wavelength ranges could be adjusted. Fortunately, it is possible to adjust wavelength ranges containing the $[O\ II]$ $\lambda 3726, 3729\text{\AA}$, $[O\ III]$ $\lambda 4363, 4959, 5007\text{\AA}$, $[S\ II]$ $\lambda 6717, 6731\text{\AA}$ emission lines, therefore at least the determination of the electron temperature $T_e(O\ III)$, the electron number density $N_e(S\ II)$ and the oxygen abundance is possible.

To derive T_e , N_e and heavy element abundances we follow the prescriptions by Izotov et al. (2006a). Namely, where possible, the coefficient of interstellar extinction $C(H\beta)$ and the equivalent width of absorption hydrogen lines EW_{abs} are derived from the observed hydrogen Balmer decrement. In this procedure we assume that EW_{abs} is the same for all hydrogen lines. Then the fluxes of emission lines were corrected for interstellar extinction and underlying stellar absorption (where this is possible).

We adopt the three zone model of the $H\ II$ region. The electron temperature $T_e(O\ III)$ in the high-ionisation zone is derived from the $[O\ III]$ $\lambda 4363/(\lambda 4959 + \lambda 5007)$ flux ratio. This temperature is used to derive abundances of ions O^{2+} and Ne^{2+} . Since $He\ II$ $\lambda 4686\text{\AA}$ emission is present in the SBS 0335–052E spectrum, the O^{3+} abundance is derived following Izotov et al. (2006a) and adopting $T_e(O\ III)$. Since the O^{3+} abundance is significantly lower than the O^{2+} abundance, the uncertainties in the temperature for the zone where the O^{3+} ion is present introduce only

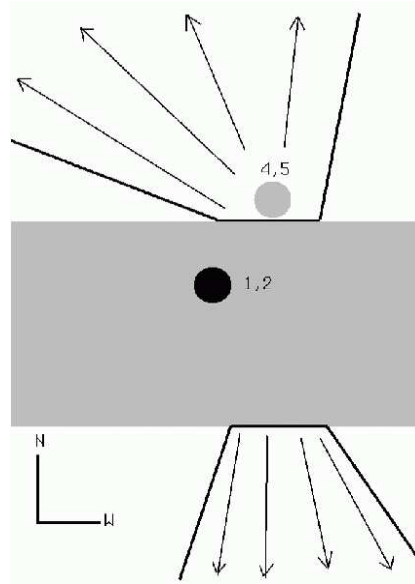


Fig. 8. Schematic $H\alpha$ kinematic model of SBS 0335–052E. Clusters 1,2 and 4,5 are shown by dark and grey circles respectively. The region with narrow $H\alpha$ profiles is shown by a grey rectangle. Its orientation is close to the orientation of the $H\ I$ cloud discussed by Pustilnik et al. (2001). Two regions with the ionised gas outflow are located to the north and south from the region with narrow $H\alpha$ emission line.

a small uncertainty in the total oxygen abundance. Some other emission lines of high-ionisation ions Ar^{3+} , Cl^{3+} , $Fe^{3+} - Fe^{6+}$ are seen in the spectrum of SBS 0335–052E in Fig. 2. In general these ions are present in the inner part of the $H\ II$ region with a temperature higher than $T_e(O\ III)$.

However, since there is no temperature constraint from observations for these ions and atomic data are not well

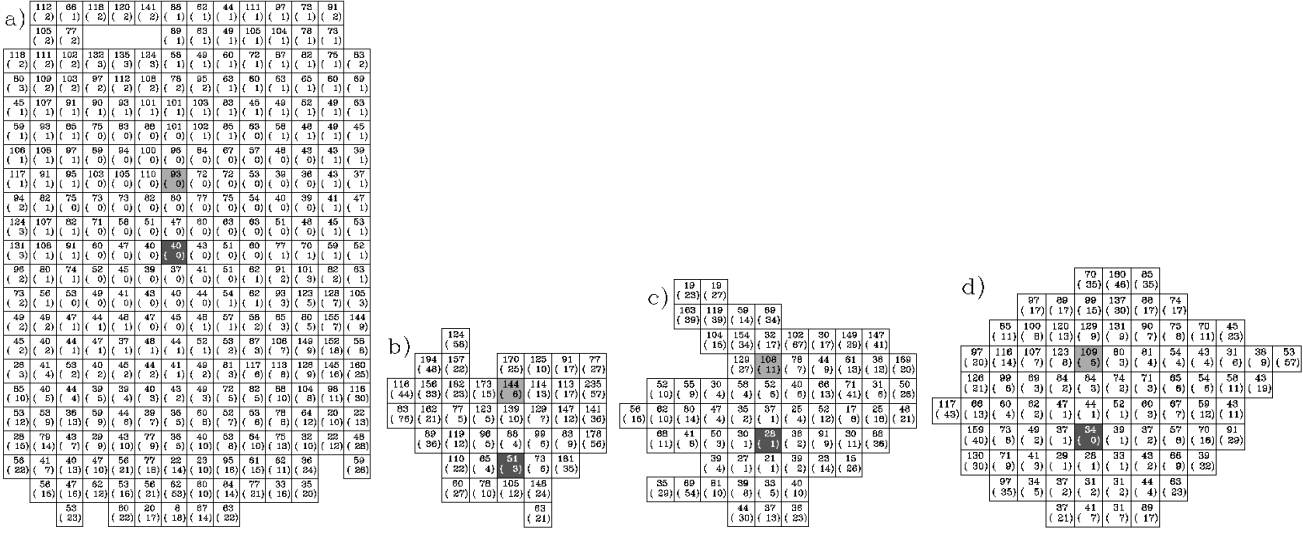


Fig. 9. Macroscopic/turbulent velocity dispersion at the FWHM (in km s^{-1}) derived from the (a) $\text{H}\alpha$ $\lambda 6563\text{\AA}$, (b) He II $\lambda 4686\text{\AA}$, (c) $[\text{O II}]$ $\lambda 3729\text{\AA}$ and (d) $[\text{O III}]$ $\lambda 4363\text{\AA}$ emission lines. The errors of the velocity dispersion are shown in parentheses. Only regions with the detected lines are shown. The dark square shows the location of clusters 1+2 with a maximum flux of $\text{H}\alpha$ 6563\AA emission line. The grey square shows the location of clusters 4+5.

known for some of them, we decided not to use these ions for the abundance determination. For the intermediate-ionisation zone we adopt the electron temperature $T_e(\text{S III})$ which was derived using the relation between $T_e(\text{S III})$ and $T_e(\text{O III})$ from Izotov et al. (2006a). The temperature $T_e(\text{S III})$ is used to derive the abundances of ions S^{2+} , Ar^{2+} and Cl^{2+} . Finally, for the low-ionisation zone we adopt the electron temperature $T_e(\text{O II})$ which was derived using the relation between $T_e(\text{O II})$ and $T_e(\text{O III})$ from Izotov et al. (2006a). This temperature is used to derive the abundances of ions O^+ , N^+ , S^+ and Fe^{2+} . Emission lines of some other low-ionisation ions and neutral species are present in the low-ionisation zone, namely, Fe^+ , O^0 , N^0 . We decided not to use them for the abundance determination since they reside both in the neutral and ionised gas and their abundances in the H II region are subject to large uncertainties.

The electron number density N_e is derived using the $[\text{O II}]$ $\lambda 3726/\lambda 3729$, $[\text{Ar IV}]$ $\lambda 4711/\lambda 4740$ and $[\text{S II}]$ $\lambda 6717/\lambda 6731$ emission line fluxes.

The total heavy element abundances are obtained with the use of ionisation correction factors ICF s from Izotov et al. (2006a) for every element. ICF s take into account the abundances of ions in unseen stages of ionisation.

5.1. Heavy Element Abundances in the Brightest Region

We first consider the chemical composition in the brightest part of SBS 0335–052E. Observed emission line fluxes relative to the $\text{H}\beta$ flux, $F(\lambda)/F(\text{H}\beta)$, emission line fluxes relative to the $\text{H}\beta$ flux, corrected for interstellar extinction and underlying stellar absorption, $I(\lambda)/I(\text{H}\beta)$, and the equivalent widths of emission lines $\text{EW}(\lambda)$ are shown

in Table 4. The extinction coefficient $C(\text{H}\beta)$, the equivalent width EW_{abs} of the absorption hydrogen Balmer lines and the observed flux $F(\text{H}\beta)$ of the $\text{H}\beta$ emission line are shown at the end of Table 4. Electron temperatures, electron number densities, ionic and total heavy element abundances for the brightest region are shown in the second column of Table 2. In general, the derived parameters are consistent with previous determinations e.g. by Izotov et al. (1997b), Izotov et al. (1999), Thuan & Izotov (2005). In particular, the electron temperature $T_e(\text{O III})$ in all measurements is high and is close to 20000K. It was found in previous studies that the H II region in SBS 0335–052E is relatively dense. We confirm this finding. The electron number density, which we derive from the $[\text{S II}]$ $\lambda 6717/\lambda 6731$ flux ratio in the brightest region, is $\sim 150 \text{ cm}^{-3}$. A similar value is obtained from the $[\text{O II}]$ $\lambda 3726/\lambda 3729$ flux ratio. On the other hand, the electron number density derived from the $[\text{Ar IV}]$ $\lambda 4711/\lambda 4740$ flux ratio, using the data from Aller (1984), is much larger, $\sim 6000 \text{ cm}^{-3}$. Thus, it appears that the high-ionisation regions are much denser than the low-ionisation regions.

The oxygen abundance $12+\log \text{O}/\text{H} = 7.31 \pm 0.01$ is in perfect agreement with recent determinations by Izotov et al. (1997b), Izotov et al. (1999) and Thuan & Izotov (2005). The Ne/O , S/O , Cl/O and Ar/O abundance ratios are very close to the average values found by, e.g., Izotov et al. (2006a) for the large sample of low-metallicity emission-line galaxies. On the other hand, the N/O abundance ratio -1.37 appears higher than the mean value of -1.5 to -1.6 for the most metal-deficient BCDs (Izotov & Thuan, 1999; Izotov et al., 2006a). Since only N^+ lines are observed in the optical spectrum of SBS 0335–052E the total nitrogen abundance is derived as $\text{N}/\text{H} = ICF(\text{N}) \times \text{N}^+/\text{H}^+$, where $ICF(\text{N}) \sim$

Table 2. Heavy Element Abundances

Property	Bright	Total
$T_e(\text{O III}), \text{K}$	20120±240	20360±480
$T_e(\text{O II}), \text{K}$	15620±170	15630±340
$T_e(\text{S III}), \text{K}$	18750±200	18910±400
$N_e(\text{O II}), \text{cm}^{-3}$	120±50	150±80
$N_e(\text{Ar IV}), \text{cm}^{-3}$	6000±2000	...
$N_e(\text{S II}), \text{cm}^{-3}$	146±41	213±74
$\text{O}^+/\text{H}^+, (\times 10^5)$	0.164±0.005	0.211±0.013
$\text{O}^{2+}/\text{H}^+, (\times 10^5)$	1.838±0.054	1.664±0.090
$\text{O}^{3+}/\text{H}^+, (\times 10^5)$	0.032±0.001	0.081±0.006
$\text{O}/\text{H}, (\times 10^5)$	2.034±0.054	1.956±0.091
$12+\log \text{O}/\text{H}$	7.31±0.01	7.29±0.02
$\text{N}^+/\text{H}^+, (\times 10^7)$	0.779±0.019	0.673±0.033
$ICF(\text{N})$	11.25	8.53
$\text{N}/\text{H}, (\times 10^7)$	8.765±0.235	5.741±0.304
$\log \text{N}/\text{O}$	-1.37±0.02	-1.53±0.03
$\text{Ne}^{2+}/\text{H}^+, (\times 10^6)$	2.977±0.092	2.941±0.199
$ICF(\text{Ne})$	1.04	1.06
$\text{Ne}/\text{H}, (\times 10^6)$	3.099±0.102	3.126±0.234
$\log \text{Ne}/\text{O}$	-0.82±0.02	-0.80±0.04
$\text{S}^+/\text{H}^+, (\times 10^7)$	0.314±0.006	0.348±0.013
$\text{S}^{2+}/\text{H}^+, (\times 10^7)$	1.539±0.052	1.433±0.136
$ICF(\text{S})$	2.36	1.93
$\text{S}/\text{H}, (\times 10^7)$	4.363±0.122	3.431±0.264
$\log \text{S}/\text{O}$	-1.67±0.02	-1.76±0.04
$\text{Cl}^{2+}/\text{H}^+, (\times 10^9)$	2.846±0.560	...
$ICF(\text{Cl})$	1.48	...
$\text{Cl}/\text{H}, (\times 10^9)$	4.207±0.827	...
$\log \text{Cl}/\text{O}$	-3.68±0.09	...
$\text{Ar}^{2+}/\text{H}^+, (\times 10^8)$	4.478±0.094	4.408±0.199
$ICF(\text{Ar})$	1.49	1.34
$\text{Ar}/\text{H}, (\times 10^8)$	6.680±0.287	5.900±0.812
$\log \text{Ar}/\text{O}$	-2.48±0.02	-2.52±0.06
$\text{Fe}^{2+}/\text{H}^+, (\times 10^7)$	0.453±0.033	...
$ICF(\text{Fe})$	17.02	...
$\text{Fe}/\text{H}, (\times 10^7)$	7.717±0.567	...
$\log \text{Fe}/\text{O}$	-1.42±0.03	...

$(\text{O}^{3+}+\text{O}^{2+}+\text{O}^+)/\text{O}^+$. Inspection of Table 4 shows that the relative flux $[\text{O II}] \lambda 3727/\text{H}\beta$ is 0.2, or 30% lower than that in some other observations of SBS 0335–052E (e.g. Izotov et al. , 1999; Papaderos et al. , 2006) resulting in high $ICF(\text{N})$. The lower $[\text{O II}] \lambda 3727$ flux in the bright region (Table 4) could be due to observational uncertainties (slightly different pointings of SBS 0335–052E during observations with different setups, effect of differential refraction, variable seeing, etc.). Adopting a $[\text{O II}] \lambda 3727$ flux $\sim 30\%$ higher will result in $\log \text{N}/\text{O} \sim -1.5$, in much better agreement with other determinations. Such increase of the $[\text{O II}] \lambda 3727$ flux will also slightly decrease by ~ 0.1 dex the iron abundance, while the abundances of other heavy elements will remain almost unchanged. In particular, the

oxygen abundance $12 + \log \text{O}/\text{H}$ will be increased only by 0.01 dex. The Fe/O abundance ratio is high and is typical for the extremely metal-deficient BCDs (Izotov et al. , 2006a). This fact suggests that the depletion of iron onto dust in SBS 0335–052E is small.

5.2. Heavy Element Abundances from the Integrated Spectrum of SBS 0335–052E

We use panoramic VLT/GIRAFFE data to obtain the integrated spectrum of SBS 0335–052E by summing every of 22×14 spectra in the whole aperture. The resulting spectrum is significantly more noisy as compared to the spectrum of the brightest region because many spectra of low-brightness regions were co-added to the spectrum of the brightest region. However, the integrated spectrum is not subject to the observational uncertainties which are much more important for the spectra obtained with the smaller apertures (non-perfect pointing, variable seeing). Additionally, it allows to obtain integrated characteristics such as the luminosity of the galaxy in individual lines.

In Table 5 are shown the measured absolute fluxes $F(\lambda)$ of the emission lines, the absolute fluxes $I(\lambda)$ corrected for the interstellar extinction and underlying stellar absorption, the respective fluxes relative to the $\text{H}\beta$ $\lambda 4861$ flux, $F(\lambda)/F(\text{H}\beta)$ and $I(\lambda)/I(\text{H}\beta)$, the equivalent widths $EW(\lambda)$ of the emission lines, the interstellar extinction coefficient $C(\text{H}\beta)$ and equivalent width of hydrogen Balmer absorption lines EW_{abs} . The absolute measured flux of $\text{H}\alpha$ emission line $F(\text{H}\alpha) = 3.45 \times 10^{-13} \text{ erg s}^{-1} \text{ cm}^{-2}$ is consistent with the value $3.23 \times 10^{-13} \text{ erg s}^{-1} \text{ cm}^{-2}$ obtained by Pustilnik et al. (2004). The luminosities of the $\text{H}\beta$ and $\text{H}\alpha$ emission lines corrected for interstellar extinction and underlying stellar absorption are equal to $L(\text{H}\beta) = 6.4 \times 10^{40} \text{ erg s}^{-1}$ and $L(\text{H}\alpha) = 1.8 \times 10^{41} \text{ erg s}^{-1}$, corresponding to the equivalent number of O7v stars $N(\text{O7v}) = 1.3 \times 10^4$. The major fraction of these stars ($\gtrsim 90\%$) is located in the two compact clusters 1 and 2 as it is evidenced by the high-resolution spatial distribution of the $\text{P}\alpha$ emission in SBS 0335–052E obtained by Thompson et al. (2006) from the HST observations. To the best of our knowledge, these two clusters (most likely, cluster 1) are among the richest super-star clusters, hosting a very large number of O stars within a region of angular size $\lesssim 0''.1 - 0''.2$, corresponding to a linear size $\lesssim 25 - 50 \text{ pc}$.

Electron temperatures, electron number densities $N_e(\text{S II})$ and $N_e(\text{O II})$, ionic and total element abundances derived from the integrated spectrum are shown in the third column of Table 2. They are similar to the parameters derived for the brightest region despite the fact that the statistical errors for the parameters derived from the integrated spectrum are higher. Note that the N/O abundance ratio derived from the integrated spectrum is lower than that derived from the spectrum of the brightest region and is consistent with the average values of N/O obtained

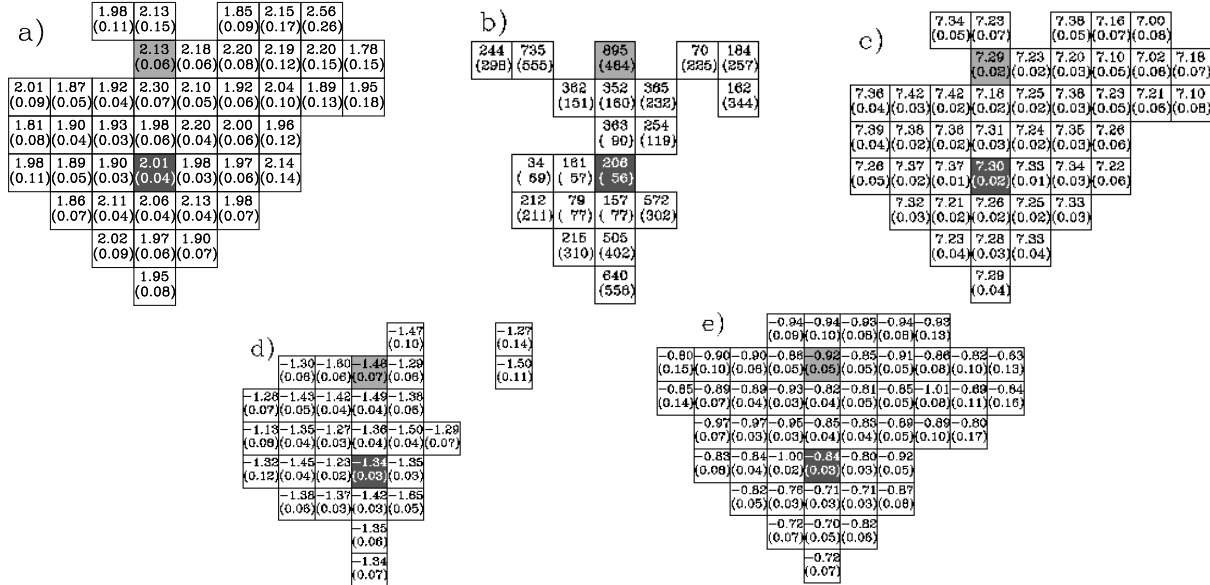


Fig. 10. (a) Electron temperature distribution (in 10^4K) from the $[\text{O III}] \lambda 4363/(\lambda 4959+\lambda 5007)$ line ratio. (b) Electron number density distribution (in cm^{-3}) from the $[\text{S II}] \lambda 6717/\lambda 6731$ line ratio. (c) Oxygen abundance $12+\log \text{O}/\text{H}$ distribution. (d) Distribution of the nitrogen-to-oxygen abundance ratio. (e) Distribution of the neon-to-oxygen abundance ratio. The dark region is the region with maximum intensity of $\text{H}\alpha$ 6563\AA emission line coincident with the location of clusters 1 and 2. The grey region corresponds to clusters 4 and 5.

for most metal-deficient galaxies (Izotov & Thuan, 1999; Izotov et al., 2006a).

5.3. Distribution of the Physical Parameters and Oxygen Abundance

The VLT/GIRAFFE panoramic spectra allow also to study the distribution of the electron temperature $T_e(\text{O III})$, the electron number density $N_e(\text{S II})$ and heavy element abundances in the H II region. For this we use the spectra obtained for the $0''.52 \times 0''.52$ apertures. We took in consideration only spectra in which at least the following lines of heavy elements are detected: $[\text{O II}] \lambda 3726, 3729\text{\AA}$, $[\text{O III}] \lambda 4363, 4959, 5007\text{\AA}$. This allows to derive the electron temperature $T_e(\text{O III})$ and oxygen abundance. From these spectra we excluded those spectra, where the oxygen abundance $12 + \log \text{O}/\text{H}$ is derived with an error greater than 0.1 dex.

In Fig. 10a is shown the distribution of the electron temperature $T_e(\text{O III})$. It is seen that the H II region is hot in all small apertures and has the characteristic temperature of $\sim 20000\text{K}$. There is a slight spatial trend of the electron temperature with $T_e(\text{O III})$ being slightly higher in the western part and slightly lower in the eastern part. The electron number density derived from the $[\text{S II}] \lambda 6717, 6731\text{\AA}$ emission lines is high, of several hundred particles per cm^3 (Fig. 10b). However, the errors in the determination of N_e are large and are caused by the low intensity of the $[\text{S II}]$ emission lines. Similar number densities are derived from the $[\text{O II}] \lambda 3726/\lambda 3729$ flux ratio. Although $[\text{O II}] \lambda 3726, 3729\text{\AA}$ emission lines are brighter than $[\text{S II}] \lambda 6717, 6731\text{\AA}$, the low signal-to-noise ratio of the spec-

trum containing $[\text{O II}]$ lines (Fig. 2) due to lower sensitivity of the GIRAFFE detector in that wavelength range prevents the determination of the electron number density from the $[\text{O II}]$ lines in a region larger than that from the $[\text{S II}]$ emission lines. As already mentioned, other emission lines detected in our spectra can in principle be used to determine the electron density. $[\text{Ar IV}] \lambda 4711$ and 4740\AA are strong enough only in the brightest region of SBS 0335–052E, where they indicate consistently an electron number density in the range $10^3 - 10^4 \text{cm}^{-3}$. $[\text{Cl III}] \lambda 5517$ and 5537\AA are too weak even in the brightest region (Fig. 2) and are therefore not used.

The oxygen abundance $12 + \log \text{O}/\text{H}$ distribution is shown in Fig. 10c. There are some variations of the oxygen abundance in the range $7.00 - 7.42$ with a slight trend of decreasing of $12 + \log \text{O}/\text{H}$ from the East to the West. In particular, it appears that the oxygen abundance in cluster 7 of ~ 7.2 (western side of Fig. 10) is slightly lower than in other clusters, confirming the finding by Papaderos et al. (2006). Thus, there is some evidence for a possible self-enrichment by heavy elements (cf. Izotov et al., 1997b, 1999) or for the presence of “initial” abundance variations in the gas. However, we point out here that the errors in the electron temperature, electron number density and oxygen abundance include only errors derived based on the photon statistics of non-flux-calibrated emission line fluxes and they do not take into account uncertainties in pointing, variable seeing, differential refraction, etc., which is difficult to estimate. Therefore, variations in the oxygen abundance may not be statistically significant.

In Fig. 10d are shown variations of N/O abundance ratio. The $\log \text{N}/\text{O}$ varies in the wide enough range from

–1.13 to –1.65 with relatively small errors. However, the real errors might be much higher because of the limitations introduced by small apertures of $0''.52 \times 0''.52$ for each spectrum. The same is true for the distribution of the Ne/O abundance ratio (Fig. 10e).

5.4. Helium Abundance from the Integrated Spectrum

SBS 0335–052E being one of the most metal-deficient BCDs plays an important role in the determination of the primordial He mass fraction Y_p and, thus, in the determination of the baryonic mass fraction of the Universe. Since the precision in the determination of Y_p should be better than $\sim 1\%$ to put useful constraints on the cosmological models, high signal-to-noise spectra are needed for this. Additionally, several systematic effects should be taken into account, and spectra and emission line fluxes should be corrected for them (see for details Izotov & Thuan, 2004; Izotov et al., 2006b). These are the corrections for (1) interstellar extinction, (2) ionisation structure, (3) collisional excitation of helium lines, (4) fluorescence in helium lines, (5) temperature variations, (6) underlying stellar absorption, (7) collisional excitation of hydrogen lines. All these corrections are at a level of a few percent and, apart from (2) influence each other in a complicated way. The case of SBS 0335–052E is particularly complicated, because its H II region is dense, hot and optically thick in some He I emission lines (Izotov et al., 1999). Therefore, effects (3), (4) and (7) are strong in the H II region of SBS 0335–052E.

To derive the He abundance we use the integrated spectrum of SBS 0335–052E because it is least dependent on the observational parameters discussed above. The He^+ abundance y^+ which is derived from the He I emission lines depends on the adopted He I emissivities. We adopt the new He I emissivities by Porter et al. (2005). In this paper, following Izotov et al. (1994, 1997a), Izotov & Thuan (1998, 2004) and Izotov et al. (2006b) we use the five strongest He I $\lambda 3889$, $\lambda 4471$, $\lambda 5876$, $\lambda 6678$ and $\lambda 7065$ emission lines to derive $N_e(\text{He}^+)$ and $\tau(\lambda 3889)$. The He I $\lambda 3889$ and $\lambda 7065$ lines play an important role because they are particularly sensitive to both quantities. Since the He I $\lambda 3889$ line is blended with the H8 $\lambda 3889$ line, we have subtracted the latter, assuming its intensity to be equal to $0.107 I(\text{H}\beta)$ (Aller, 1984).

Besides the emissivities the derived $y^+ \equiv \text{He}^+/\text{H}^+$ abundance depends on several other parameters: collisional excitation of hydrogen emission lines, electron number density $N_e(\text{He}^+)$ and electron temperature $T_e(\text{He}^+)$, equivalent widths $\text{EW}(\lambda 3889)$, $\text{EW}(\lambda 4471)$, $\text{EW}(\lambda 5876)$, $\text{EW}(\lambda 6678)$ and $\text{EW}(\lambda 7065)$ of He I stellar absorption lines, optical depth $\tau(\lambda 3889)$ of the He I $\lambda 3889$ emission line. We use Monte Carlo simulations for the y^+ determination randomly varying the parameters in their ranges. First, we subtract the fractions of the H α and H β observed fluxes due to the collisional excitation. We adopt that the fraction $\Delta I_{\text{coll}}(\text{H}\alpha)/I(\text{H}\alpha)$ of the H α flux due to the col-

lisional excitation varies in the range 0% – 5% of the total flux. This fraction is randomly generated 100 times in the adopted range. The fraction of the H β emission line flux due to the collisional excitation is adopted to be three times less than that of the H α flux. For each generated fraction of the H α and H β they are subtracted from the total observed fluxes and then all emission line fluxes are corrected for the interstellar extinction and abundances of elements are calculated.

To calculate y^+ we simultaneously and randomly vary $N_e(\text{He}^+)$, $T_e(\text{He}^+)$ and $\tau(\lambda 3889)$. The total number of such realizations is 10^5 for each value of $\Delta I_{\text{coll}}(\text{H}\alpha)/I(\text{H}\alpha)$. Thus, the total number of Monte Carlo realizations is $100 \times 10^5 = 10^7$. As for He I underlying stellar absorption, we keep constant values of $\text{EW}(\lambda 3889)$, $\text{EW}(\lambda 4471)$, $\text{EW}(\lambda 5876)$, $\text{EW}(\lambda 6678)$ and $\text{EW}(\lambda 7065)$ during simulations. In our spectrum other He I emission lines, namely He I $\lambda 3820$, $\lambda 4388$, $\lambda 4026$, $\lambda 4921$, and $\lambda 7281$ are seen. However, we do not attempt to use these lines for He abundance determination because they are much weaker as compared to the five brightest lines, and hence have larger uncertainties.

We solve the problem by minimization of the expression

$$\chi^2 = \sum_i^n \frac{(y_i^+ - y_{\text{mean}}^+)^2}{\sigma^2(y_i^+)}, \quad (2)$$

where y_i^+ is the He^+ abundance derived from the flux of the He I emission line with label i , $\sigma(y_i^+)$ is the statistical error of the He abundance. The quantity y_{mean}^+ is the weighted mean of the He^+ abundance as derived from the equation

$$y_{\text{mean}}^+ = \frac{\sum_i^k y_i^+ / \sigma^2(y_i^+)}{\sum_i^k 1 / \sigma^2(y_i^+)}. \quad (3)$$

We use all five He I emission lines to calculate χ^2 (i.e., $n = 5$), but only three lines, He I $\lambda 4471$, He I $\lambda 5876$ and He I $\lambda 6678$ to calculate y_{mean}^+ ($k = 3$). This is because the fluxes of He I $\lambda 3889$ and He I $\lambda 7065$ emission lines are more uncertain compared to other three He I emission lines.

The best solution for y_{mean}^+ is found from the minimum of χ^2 , the systematic error σ_{sys} is obtained from the dispersion of y_{mean}^+ in the range of χ^2 between χ_{min}^2 and $\chi_{\text{min}}^2 + 1$. Then the total error for y_{mean}^+ is derived from $\sigma_{\text{tot}}^2 = \sigma_{\text{stat}}^2 + \sigma_{\text{sys}}^2$.

Additionally, since the nebular He II $\lambda 4686\text{\AA}$ emission line was detected, we have added the abundance of doubly ionised helium $y^{2+} \equiv \text{He}^{2+}/\text{H}^+$ to y^+ . Although the He^{2+} zone is hotter than the He^+ zone, we adopt $T_e(\text{He}^{2+}) = T_e(\text{He}^+)$. The last assumption introduces a little change in y value, because the value of y^{2+} is small ($\sim 4\%$ of y^+). Finally, the ionisation correction factor $ICF(\text{He})$ is taken into account from Izotov et al. (2006b) to convert $y^+ + y^{2+}$ to the total He abundance $y \equiv \text{He}/\text{H}$.

The derived parameters and He abundances for every He I emission line are shown in Table 3. Here,

Table 3. Helium Abundance

Parameter	Value
$T_e(\text{O III})$, K	20180
$T_e(\text{He}^+)$, K	20010
$N_e(\text{He}^+)$, cm^{-3}	295
$\text{EW}_{abs}(\lambda 4471)$, Å	0.4
$\text{EW}_{abs}(\lambda 3889)/\text{EW}_{abs}(\lambda 4471)$	1.0
$\text{EW}_{abs}(\lambda 5876)/\text{EW}_{abs}(\lambda 4471)$	0.3
$\text{EW}_{abs}(\lambda 6678)/\text{EW}_{abs}(\lambda 4471)$	0.1
$\text{EW}_{abs}(\lambda 7065)/\text{EW}_{abs}(\lambda 4471)$	0.1
$\tau(\lambda 3889)$	2.9
$\Delta I_{coll}(\text{H}\alpha)/I(\text{H}\alpha)$, %	4.95
χ^2_{min}	0.1825
$y^+(\lambda 3889)$	0.0782 ± 0.0134
$y^+(\lambda 4471)$	0.0802 ± 0.0032
$y^+(\lambda 5876)$	0.0788 ± 0.0012
$y^+(\lambda 6678)$	0.0787 ± 0.0018
$y^+(\lambda 7065)$	0.0789 ± 0.0018
$y^+(\text{weighted mean})$	0.0789 ± 0.0010
$y^{++}(\lambda 4686)$	0.0034 ± 0.0002
$ICF(\text{He})$	0.993
$y(\text{weighted mean})$	0.0817 ± 0.0010
$Y(\text{weighted mean})$	0.2463 ± 0.0030

$\Delta I_{coll}(\text{H}\alpha)/I(\text{H}\alpha)$ is the fraction of $\text{H}\alpha$ flux due to the collisional excitation. It is seen from this Table, that the electron number density N_e in the He^+ zone is high, 295 cm^{-3} , and is consistent with the number density derived from the [S II] emission lines. The electron temperature $T_e(\text{O III})$ in Table 3 slightly differs from that in Table 2 (right column). This is because in Table 3 collisional excitation of hydrogen lines is taken into account resulting in smaller $C(\text{H}\beta)$ as compared to that in Table 2. The electron temperature $T_e(\text{He}^+)$ is only slightly lower than $T_e(\text{O III})$ suggesting that temperature fluctuations in the H II region of SBS 0335–052E are small. Note, that the optical depth $\tau(\lambda 3889)$ of 2.9 is high compared to that in other BCDs (see e.g. Izotov & Thuan, 2004) implying important contribution of the fluorescent enhancement of He I emission lines.

The derived weighted mean He mass fraction in SBS 0335–052E, $Y = 0.2463 \pm 0.0030$, is slightly lower (but consistent within the errors) than the primordial He mass fraction $Y_p = 0.24815 \pm 0.0003 \pm 0.0006(\text{syst.})$ from the 3-year data of the WMAP experiment (Spergel et al., 2006) and the D abundance, supporting the standard cosmological model of the primordial nucleosynthesis.

6. Wolf-Rayet Stars

The search for Wolf-Rayet (WR) stars in extremely low-metallicity dwarf galaxies is of great interest for constraining stellar evolution models. However, such studies are difficult since the strength of WR emission lines is significantly reduced with decreasing metallicity. Therefore, very high signal-to-noise ratio spectra are required to detect weak WR features. For a long time no WR galaxies with an oxygen abundance $12 + \log \text{O}/\text{H} < 7.9$ were known

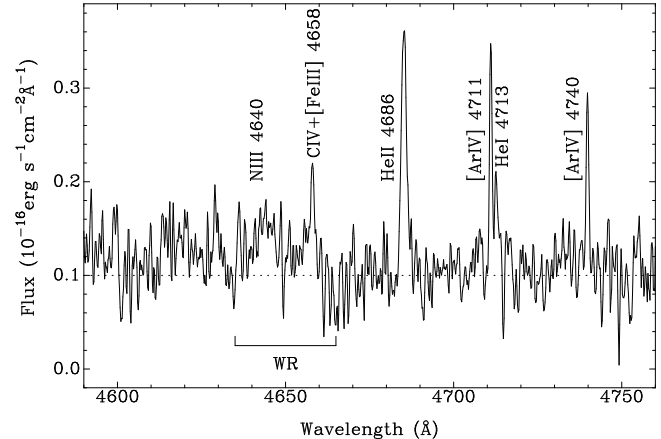


Fig. 11. Part of the spectrum of cluster 3 showing the probable broad Wolf-Rayet emission lines N III $\lambda 4640$ and C IV $\lambda 4658$ labelled “WR”.

(Masegosa et al., 1991). Later, Izotov et al. (1997c) and Legrand et al. (1997) have discovered WR stars in I Zw 18, at that time the most metal-deficient emission-line galaxy with the oxygen abundance $12 + \log \text{O}/\text{H} = 7.17$. Thus, it appears that WR stars could be found in any other dwarf emission-line galaxy with active star formation, including SBS 0335–052E. However, the strength of WR emission features depends not only on metallicity but also on the age of a starburst. In starbursts with the metallicity of SBS 0335–052E, the WR stage is expected to be very short, typically less than 1 Myr (Schaerer & Vacca, 1998; de Mello et al., 1998). Therefore, not all young clusters ionising the interstellar medium in SBS 0335–052E may be expected to contain WR stars. Recently, Papaderos et al. (2006) have found that WR stars of the early carbon sequence (WC4 stars) are present in cluster 3 of SBS 0335–052E.

GIRAFFE/ARGUS observations allow in principle a more detailed search for WR stars in SBS 0335–052E, a more precise localisation in the galaxy, and also to resolve the $\lambda 4650$ WR bump into N III $\lambda 4640$ and C IV $\lambda 4658$ broad features, thus allowing the detection of both late nitrogen WR stars (WNL stars) and early carbon WR stars (WCE stars). Previous observations by Papaderos et al. (2006) had too low spectral resolution to definitely distinguish between two types of WR stars. However, there are some limitations of GIRAFFE/ARGUS observations which make such study more difficult as compared with that of Papaderos et al. (2006). Although Papaderos et al. (2006) have observed with the smaller 3.6m ESO telescope, their spectrum has a higher S/N ratio because of the ~ 3 times longer exposure and ~ 10 times lower spectral resolution.

We checked all $0''.52 \times 0''.52$ spectra obtained with GIRAFFE and found that broad WR features near $\lambda 4650$ are likely present only in one spectrum associated with cluster 3. This spectrum is shown in Fig. 11. The S/N ratio of ~ 5 of this spectrum is not high, but broad WR features are clearly seen. Thus, we confirm the finding

by Papaderos et al. (2006) that WR stars appear to be present in cluster 3. However, we find that the WR feature consists in fact of two lines: N III $\lambda 4640$ and C IV $\lambda 4658$. The latter line is blended with the much narrower nebular [Fe III] $\lambda 4658$ emission line. We find that, after subtraction of the [Fe III] line from the $\lambda 4658$ blend, the fluxes of the N III $\lambda 4640$ and C IV $\lambda 4658$ lines and their FWHMs are similar, $\sim (4 \pm 1) \times 10^{-17}$ erg s $^{-1}$ cm $^{-2}$ and 6.5 Å, respectively. Thus, the total flux of the $\lambda 4650$ bump (N III $\lambda 4640$ + C IV $\lambda 4658$) non-corrected for extinction is $\sim 8 \times 10^{-17}$ erg s $^{-1}$ cm $^{-2}$, or 2/3 that measured by Papaderos et al. (2006) in a larger aperture. The total equivalent width of this bump is EW($\lambda 4650$) ~ 9 Å. The C IV $\lambda 4658$ emission line should be accompanied by the C IV $\lambda 5808$ emission line with a comparable flux. Unfortunately, the redshifted C IV $\lambda 5808$ emission line in SBS 0335–052E coincides with the night sky Na I $\lambda 5890$, $\lambda 5895$ emission lines. Therefore, the imperfect night sky subtraction hinders the detection of the WR line.

The observed (i.e. not extinction corrected) N III $\lambda 4640$ and C IV $\lambda 4658$ emission line luminosities of cluster 3 are equal to $L(\text{N III } \lambda 4640) = L(\text{C IV } \lambda 4658) = 1.4 \times 10^{37}$ erg s $^{-1}$ and correspond to the number of WNL and stars $N(\text{WNL}) \sim 35 \pm 8$ and to the number of WC4 stars $N(\text{WC4}) \sim 3 \pm 1$ if we adopt the “standard” WR line luminosities computed by Schaerer & Vacca (1998), i.e. assuming N III $\lambda 4640$ and C IV $\lambda 4658$ emission line luminosities of 4×10^{35} erg s $^{-1}$ and 5×10^{36} erg s $^{-1}$ respectively for a single WNL and WC4 star. The derived values of WNL and WC4 stars are to be taken with a grain of salt for various reasons. First these are likely lower limits because of the neglected reddening, and since WR stars at low metallicity may have lower intrinsic line luminosities (e.g. Crowther & Hadfield, 2006). Second, it is not necessarily clear that the observed lines are indeed due to WN and WC stars, as their strengths and widths are somewhat unusual. Their relatively small widths could be due to lower mass loss rates and/or smaller wind velocities in WR stars at such low metallicity (Crowther et al., 2002; Vink & de Koter, 2005; Crowther & Hadfield, 2006). Alternatively, from their relative strength and the small widths, the observed lines could also correspond to very late WNL stars (WN 10h–11h) (cf. Crowther & Smith, 1997), if most of the C IV $\lambda 4658$ was nebular. Given the faintness of these spectral signatures and the lack of known individual WR stars at such low metallicities as comparison objects, it is difficult to draw firm conclusions on the WR content in this cluster.

7. Conclusions

In this paper we present panoramic spectroscopic observations with the VLT/GIRAFFE in the spectral range $\lambda 3620$ – 9400 Å of one of the most metal-deficient blue compact dwarf (BCD) galaxies, SBS 0335–052E. Our findings can be summarized as follows:

1. The morphology of the galaxy in different lines is very similar, except for the He II $\lambda 4686$ Å line, suggesting that the main ionising source in this galaxy is the compact super-star clusters (SSC) 1+2 in the SE part of the galaxy, most likely the cluster 1. The equivalent number of O7v ionising stars in this cluster is ~ 13000 , making it the most powerful SSC known so far.

2. The maximum emission of the He II $\lambda 4686$ Å line is offset to the older compact clusters 4 and 5. Additionally, its width is 1.5 – 2 times greater than the width of other lines. Furthermore, the width of this and other emission lines is much higher in clusters 4,5 than in cluster 1. These facts imply that the hard ionising radiation responsible for He II emission is most likely produced by fast radiative shocks. However, some contribution from WR stars located in cluster 3 cannot be excluded.

3. The analysis of kinematical properties of the ionised gas in SBS 0335–052E suggests the presence of gas outflow in the direction perpendicular to the galaxy disk.

4. We derive physical parameters in the H II region of SBS 0335–052E, suggesting that the ionised gas is hot (~ 20000 K) and dense (\gtrsim several hundred particles per cm $^{-3}$). The oxygen abundances $12 + \log \text{O}/\text{H}$ in the brightest region and in the integrated spectrum of SBS 0335–052E are respectively 7.31 ± 0.01 and 7.29 ± 0.02 , and they are consistent with previous determinations. The other heavy element-to-oxygen abundance ratios are consistent with the average values derived for other most metal-deficient galaxies. There is a slight decrease of oxygen abundance from the East to the West suggesting some self-enrichment of the ionised gas by heavy elements.

5. We derive the He mass fraction Y from the integrated spectrum taking into account all possible systematic effects in the He abundance determination. Our value $Y = 0.2463 \pm 0.0030$ is slightly lower but consistent within the errors with the primordial He mass fraction determined from the 3 year WMAP data and from primordial deuterium measurements.

6. We confirm the presence of Wolf-Rayet stars in the cluster 3 found previously by Papaderos et al. (2006). The lower limits of the WNL and WC4 star numbers are $\sim 35 \pm 8$ and $\sim 3 \pm 1$, respectively if standard WR line luminosities are assumed.

Acknowledgements. Y. I. I. and N. G. G. thank the hospitality of the Observatoire de Genève. DS thanks Paul Crowther for useful comments on WR stars and the Swiss National Science Foundation for support.

References

- Aller, L. H. 1984, Physics of Thermal Gaseous Nebulae (Dordrecht: Reidel)
- Blecha, A., Cayatte, V., North, P., Royer, F., & Simond, G. 2000, in Proc. SPIE Vol. 4008, Optical and IR Telescope Instrumentation and Detectors, Eds. Iye M. & Moorwood A. F., p. 467
- Crowther, P. A., Dessart, L., Hillier, D.J., Abbott, J.B., & Fullerton, A.W., 2002, A&A, 392, 653

- Crowther, P. A., & Hadfield, L. J., 2006, *A&A*, 449, 711
- Crowther, P. A., & Smith, L. J., 1997, *A&A*, 320, 500
- de Mello, D., Schaerer, D., Heldmann, J., & Leitherer, C., 1999, *A&A*, 507, 199
- Fricke, K. J., Izotov, Y. I., Papaderos, P., Guseva, N. G., & Thuan, T. X. 2001, *AJ*, 121, 169
- Garnett, D. R., et al., 1991, *ApJ*, 373, 458
- Houck, J. R., Charmandaris, V., Brandl, B. R., et al. 2004, *ApJS*, 154, 211
- Hunt, L. K., Vanzì, L., & Thuan, T. X. 2001, *A&A*, 377, 66
- Izotov, Y. I., & Thuan, T. X. 1998, *ApJ*, 500, 188
- Izotov, Y. I., & Thuan, T. X. 1999, *ApJ*, 511, 639
- Izotov, Y. I., & Thuan, T. X. 2004, *ApJ*, 602, 200
- Izotov, Y. I., Guseva, N. G., Lipovetsky, V. A., Kniazev, A. Y., & Stepanian, J. A. 1990, *Nature*, 343, 238
- Izotov, Y. I., Thuan, T. X., & Lipovetsky, V. A. 1994, *ApJ*, 435, 647
- Izotov, Y. I., Thuan, T. X., & Lipovetsky, V. A. 1997a, *ApJS*, 108, 1
- Izotov, Y. I., Chaffee, F. H., Foltz, C. B., Green, R. F., Guseva, N. G., & Thuan, T. X. 1999, *ApJ*, 527, 757
- Izotov, Y. I., Lipovetsky, V. A., Chaffee, F. H., Foltz, C. B., Guseva, N. G., & Kniazev, A. Y. 1997b, *ApJ*, 476, 698
- Izotov, Y. I., Foltz, C. B., Green, R. F., Guseva, N. G., & Thuan, T. X. 1997c, *ApJ*, 487, L37
- Izotov, Y. I., Chaffee, F. H., & Schaerer, D. 2001b, *A&A*, 378, L45
- Izotov, Y. I., Noeske, K. G., Guseva, N. G., Papaderos, P., Thuan, T. X., & Fricke, K. J. 2004, *A&A*, 415, L27
- Izotov, Y. I., Thuan, T. X., & Guseva, N. G. 2005, *ApJ*, 415, 87
- Izotov, Y. I., Stasińska, G., Meynet, G., Guseva, N. G., & Thuan, T. X. 2006a, *A&A*, 448, 955
- Izotov, Y. I., Thuan, T. X., & Stasińska, G. 2006b, in preparation
- Kunth, D., Leitherer, C., Mas-Hesse, J. M., Östlin, G., & Petrosian, A. 2003, *ApJ*, 597, 263
- Legrand, F., Kunth, D., Roy, J.-R., Mas-Hesse, J. M., & Walsh, J. R. 1997, *A&A*, 326, L17
- Masegosa, J., Moles, M., & del Olmo, A. 1991, *A&A*, 249, 505
- Melnick, J., Heydari-Malayeri, M., & Leisy, P. 1992, *A&A*, 253, 16
- Papaderos, P., Izotov, Y. I., Fricke, K. J., Thuan, T. X., & Guseva, N. G. 1998, *A&A*, 338, 43
- Papaderos, P., Izotov, Y. I., Guseva, N. G., Thuan, T. X., & Fricke, K. J. 2006, *A&A*, in press; preprint astro-ph/0604270
- Pasquini, L., Avila, G., Blecha, A., et al. 2002, *ESO Messenger*, 110, 1
- Petrosian, A. R., Boulesteix, J., Comte, G., Kunth, D., & LeCoarer, E. 1997, *A&A*, 318, 390
- Porter, R. L., Bauman, R. P., Ferland, G. J., & MacAdam, K. B. 2005, *ApJ*, 622, L73
- Pustilnik, S. A., Lipovetsky, V. A., Izotov, Y. I., et al. 1997, *Ast.L.*, 23, 308
- Pustilnik, S. A., Brinks, E., Thuan, T. X., Lipovetsky, V. A., & Izotov, Y. I. 2001, *AJ*, 121, 1413
- Pustilnik, S. A., Pramskij, A. G., & Kniazev, A. Y. 2004, *A&A*, 425, 51
- Royer, F., Blecha, A., North, P., Simond, G., Baratchart, S., Cayatte, V., Chemin, L., & Palsa, R. 2002, in *Proc. SPIE Vol. 4847, Astronomical Data Analysis II.*, Eds. Stark J.-L. & Murtagh F. D., p. 184
- Schaerer, D., 1996, *ApJ*, 467, L17
- Schaerer, D., & Vacca, W. D. 1998, *ApJ*, 497, 618
- Spergel, D., et al., 2006, *ApJ*, submitted; preprint astro-ph/0603449
- Thompson, R. I., Sauvage, M., Kennicutt, R. C., Jr., Engelbracht, C. W., & Vanzì, L. 2006, *ApJ*, 638, 176
- Thuan, T. X., & Izotov, Y. I. 1997, *ApJ*, 489, 623
- Thuan, T. X., & Izotov, Y. I. 2005, *ApJS*, 161, 240
- Thuan, T. X., Izotov, Y. I., & Lipovetsky, V. A. 1997, *ApJ*, 477, 661
- Thuan, T. X., Sauvage, M., & Madden, S. 1999, *ApJ*, 516, 783
- Thuan, T. X., Bauer, F. E., Papaderos, P., & Izotov, Y. I. 2004, *ApJ*, 606, 213
- Thuan, T. X., Lecavelier des Etangs, A., & Izotov, Y. I. 2005, *ApJ*, 621, 269
- Vanzì, L., Hunt, L. K., Thuan, T. X., & Izotov, Y. I. 2000, *A&A*, 363, 493
- Vink, J.S., & de Koter, A., 2005, *A&A*, 442, 587
- Whitford, A. E. 1958, *AJ*, 63, 201

Online Material

Table 4. Emission Line Fluxes and Equivalent Widths in the Spectrum of the Brightest Region

Line	$100 \times F(\lambda)/F(\text{H}\beta)$	$100 \times I(\lambda)/I(\text{H}\beta)$	$EW(\lambda)^a$
LR1 ($\lambda 3620\text{--}4081$)			
3634 He I	0.25±0.02	0.29±0.13	0.33±0.04
3631 H24	0.47±0.02	1.08±0.23	0.89±0.06
3674 H23	0.59±0.03	1.21±0.20	1.13±0.07
3676 H22	0.60±0.03	1.21±0.19	1.19±0.07
3679 H21	0.80±0.04	1.36±0.15	1.86±0.08
3683 H20	1.16±0.04	1.76±0.13	2.85±0.10
3687 H19	0.83±0.04	1.33±0.13	2.28±0.10
3692 H18	1.08±0.04	1.62±0.12	2.90±0.09
3697 H17	1.07±0.04	1.70±0.14	2.31±0.10
3704 H16	1.40±0.04	2.06±0.12	3.17±0.09
3705 He I	0.59±0.03	0.68±0.08	1.37±0.08
3712 H15	1.21±0.04	1.83±0.13	2.81±0.09
3722 H14	1.80±0.05	2.53±0.13	3.90±0.10
3726 [O II]	8.12±0.13	9.26±0.18	17.73±0.14
3729 [O II]	9.51±0.15	10.85±0.20	20.86±0.17
3734 H13	2.01±0.05	2.76±0.13	4.46±0.13
3750 H12	2.75±0.07	3.59±0.14	6.12±0.15
3771 H11	3.08±0.08	3.96±0.15	6.65±0.14
3798 H10	4.03±0.10	5.04±0.17	8.45±0.19
3820 He I	0.72±0.07	0.81±0.11	1.63±0.17
3835 H9	6.19±0.15	7.37±0.20	15.35±0.29
3868 [Ne III]	21.29±0.36	23.84±0.43	47.27±0.45
3889 He I+H8	14.13±0.29	16.22±0.36	32.49±0.50
3965 He I	0.61±0.23	0.68±0.26	1.60±0.58
3967 [Ne III]	6.51±0.29	7.20±0.33	18.31±0.70
3970 H7	14.02±0.42	15.85±0.50	39.08±0.93
LR2 ($\lambda 3964\text{--}4567$)			
3965 He I	0.64±0.01	0.71±0.08	1.30±0.04
3967 [Ne III]	7.16±0.11	7.91±0.15	14.64±0.08
3970 H7	13.97±0.20	15.92±0.26	28.70±0.10
4026 He I	1.60±0.03	1.75±0.09	3.38±0.05
4068 [S II]	0.25±0.02	0.28±0.08	0.54±0.04
4101 H δ	23.99±0.35	26.53±0.42	51.74±0.16
4121 He I	0.24±0.02	0.26±0.08	0.52±0.05
4144 He I	0.41±0.03	0.44±0.08	0.89±0.06
4169 He I	0.10±0.02	0.10±0.08	0.21±0.05
4227 [Fe V]	0.20±0.03	0.21±0.08	0.45±0.08
4249 [Fe II]	0.07±0.02	0.08±0.07	0.17±0.05
4287 [Fe II]	0.16±0.02	0.17±0.07	0.39±0.07
4340 H γ	46.80±0.68	49.82±0.75	114.10±0.33
4359 [Fe II]	0.17±0.03	0.18±0.06	0.59±0.07
4363 [O III]	10.52±0.17	11.08±0.19	25.39±0.18
4368 O I	0.10±0.03	0.11±0.07	0.25±0.06
4379 N III	0.10±0.03	0.10±0.07	0.24±0.08
4388 He I	0.44±0.03	0.46±0.07	1.10±0.10
4414 [Fe II]	0.08±0.02	0.08±0.07	0.19±0.07
4416 [Fe II]	0.05±0.02	0.05±0.06	0.13±0.07
4438 He I	0.11±0.03	0.12±0.07	0.29±0.08
4471 He I	3.75±0.08	3.90±0.10	9.83±0.15
LR3 ($\lambda 4501\text{--}5078$)			
4452 [Fe II]	0.10±0.01	0.10±0.06	0.25±0.04
4471 He I	3.75±0.06	3.90±0.09	9.88±0.08
4541 He II	0.05±0.01	0.05±0.06	0.13±0.04
4571 Mg I	0.09±0.01	0.10±0.06	0.26±0.04

Table 4. Continued.

Line	$100 \times F(\lambda)/F(H\beta)$	$100 \times I(\lambda)/I(H\beta)$	$EW(\lambda)^a$
4658 [Fe III]	0.26±0.02	0.26±0.06	0.75±0.05
4686 He II	1.39±0.03	1.41±0.06	4.36±0.08
4702 [Fe III]	0.12±0.01	0.12±0.05	0.39±0.05
4711 [Ar IV]	1.08±0.02	1.09±0.06	3.34±0.06
4713 He I	0.70±0.02	0.70±0.05	2.14±0.06
4734 [Fe III]	0.04±0.01	0.04±0.05	0.13±0.04
4740 [Ar IV]	0.95±0.03	0.96±0.06	3.04±0.08
4861 H β	100.00±1.43	100.00±1.44	321.70±0.46
4881 [Fe III]	0.10±0.02	0.10±0.05	0.31±0.06
4893 [Fe VII]	0.04±0.01	0.04±0.05	0.14±0.05
4907 [Fe IV]	0.11±0.02	0.11±0.05	0.41±0.05
4921 He I	1.04±0.03	1.03±0.05	4.05±0.11
4930 [Fe III]	0.09±0.02	0.09±0.04	0.34±0.06
4959 [O III]	107.82±1.54	106.45±1.53	406.70±0.53
4972 [Fe VI]	0.11±0.02	0.10±0.04	0.41±0.07
4986 [Fe III]	0.41±0.03	0.40±0.05	1.48±0.08
5007 [O III]	333.72±4.75	327.89±4.70	1075.00±0.75
LR4 (λ 5010–5831)			
4959 [O III]	107.84±1.54	106.46±1.53	317.50±0.32
4986 [Fe III]	0.41±0.02	0.41±0.05	1.37±0.06
5007 [O III]	325.05±4.62	319.37±4.57	912.80±0.57
5016 He I	2.01±0.04	1.97±0.06	5.99±0.08
5041 Si II	0.15±0.02	0.14±0.05	0.51±0.05
5048 He I	0.21±0.02	0.21±0.05	0.74±0.07
5147 [Fe VI]	0.06±0.03	0.05±0.05	0.19±0.06
5158 [Fe VII]	0.05±0.02	0.05±0.05	0.18±0.06
5176 [Fe VI]	0.11±0.02	0.11±0.05	0.42±0.08
5198 [N I]	0.21±0.02	0.20±0.05	0.74±0.09
5200 [N I]	0.09±0.02	0.08±0.04	0.31±0.08
5261 [Fe II]	0.06±0.02	0.06±0.04	0.21±0.06
5270 [Fe III]	0.18±0.03	0.17±0.05	0.64±0.10
5273 [Fe II]	0.02±0.01	0.02±0.04	0.09±0.06
5323 [Cl IV]	0.05±0.03	0.04±0.05	0.17±0.09
5335 [Fe VI]	0.03±0.02	0.03±0.04	0.12±0.09
5411 He II	0.14±0.03	0.13±0.04	0.52±0.11
5517 [Cl III]	0.11±0.03	0.10±0.05	0.43±0.11
5537 [Cl III]	0.08±0.02	0.07±0.04	0.31±0.11
5631 [Fe VI]	0.02±0.02	0.02±0.04	0.08±0.10
5639 [Fe VI]	0.03±0.04	0.03±0.05	0.12±0.09
5721 [Fe VII]	0.05±0.03	0.04±0.04	0.21±0.13
LR5 (λ 5741–6524)			
5755 [N II]	0.05±0.01	0.05±0.03	0.24±0.03
5876 He I	10.18±0.15	9.25±0.14	47.95±0.13
5957 Si II	0.04±0.01	0.03±0.03	0.19±0.03
5979 Si II	0.06±0.01	0.05±0.03	0.29±0.03
6046 O I	0.05±0.01	0.05±0.03	0.27±0.04
6102 He II	0.04±0.01	0.03±0.03	0.21±0.04
6118 He II	0.01±0.01	0.01±0.02	0.08±0.03
6133 [Fe III]	0.02±0.01	0.02±0.02	0.11±0.03
6300 [O I]	0.74±0.02	0.65±0.03	4.10±0.06
6312 [S III]	0.64±0.02	0.56±0.03	3.67±0.07
6348 Si II	0.08±0.01	0.07±0.02	0.46±0.04
6363 [O I]	0.27±0.01	0.24±0.02	1.58±0.05
6371 Si II	0.09±0.01	0.08±0.02	0.55±0.05

Table 4. Continued.

Line	$100 \times F(\lambda)/F(H\beta)$	$100 \times I(\lambda)/I(H\beta)$	$EW(\lambda)^a$
LR6 ($\lambda 6438-7184$)			
6363 [O I]	0.28±0.01	0.25±0.03	1.50±0.05
6371 Si II	0.09±0.01	0.08±0.03	0.47±0.05
6548 [N II]	0.44±0.01	0.38±0.03	1.98±0.05
6563 H α	317.90±4.52	274.31±4.26	1427.00±0.77
6583 [N II]	1.33±0.02	1.14±0.04	6.23±0.07
6678 He I	3.07±0.05	2.63±0.05	17.76±0.12
6717 [S II]	2.27±0.04	1.94±0.04	13.41±0.11
6731 [S II]	1.77±0.03	1.51±0.04	10.49±0.10
6739 [Fe III]	0.06±0.01	0.05±0.02	0.33±0.05
7002 O I	0.07±0.01	0.06±0.02	0.47±0.05
7065 He I	5.98±0.09	4.99±0.09	38.51±0.19
LR7 ($\lambda 7102-8343$)			
7065 He I	5.98±0.09	4.99±0.09	31.85±0.13
7136 [Ar III]	1.93±0.03	1.60±0.04	11.48±0.10
7171 [Ar IV]	0.09±0.01	0.08±0.02	0.59±0.06
7237 [Ar IV]	0.06±0.01	0.05±0.02	0.37±0.06
7254 O I	0.11±0.01	0.09±0.02	0.68±0.07
7263 [Ar IV]	0.04±0.01	0.03±0.02	0.25±0.06
7281 He I	0.84±0.02	0.70±0.03	5.38±0.10
7320 [O II]	0.69±0.02	0.57±0.02	4.47±0.10
7330 [O II]	0.61±0.02	0.50±0.02	4.06±0.10
7468 N I	0.04±0.01	0.03±0.02	0.26±0.07
7751 [Ar III]	0.57±0.02	0.46±0.02	4.18±0.12
7816 He I	0.13±0.01	0.11±0.02	0.96±0.10
8046 [Cl IV]	0.08±0.01	0.07±0.02	0.64±0.11
LR8 ($\lambda 8206-9400$)			
8223 N I	0.06±0.01	0.05±0.02	0.52±0.08
8281 P32	0.09±0.01	0.14±0.05	0.77±0.09
8298 P28	0.10±0.01	0.16±0.04	0.90±0.09
8306 P27	0.09±0.01	0.15±0.05	0.87±0.09
8314 P26	0.16±0.01	0.20±0.03	1.51±0.10
8323 P25	0.15±0.01	0.19±0.04	1.38±0.11
8334 P24	0.28±0.01	0.30±0.03	2.53±0.10
8346 P23	0.16±0.01	0.20±0.03	1.52±0.09
8359 P22	0.31±0.01	0.32±0.02	2.89±0.11
8362 He I	0.14±0.01	0.11±0.01	1.29±0.09
8374 P21	0.37±0.01	0.35±0.02	3.76±0.13
8392 P20	0.39±0.01	0.38±0.02	3.53±0.12
8413 P19	0.38±0.01	0.38±0.02	3.40±0.12
8438 P18	0.39±0.01	0.38±0.02	3.40±0.11
8446 O I	0.84±0.02	0.65±0.02	7.11±0.14
8467 P17	0.58±0.02	0.53±0.02	5.09±0.12
8502 P16	0.59±0.01	0.54±0.02	5.01±0.14
8545 P15	0.75±0.02	0.67±0.03	5.62±0.11
8598 P14	0.88±0.02	0.77±0.03	6.73±0.13
8664 P13	1.03±0.02	0.89±0.03	7.07±0.11
8751 P12	1.43±0.03	1.18±0.03	11.98±0.15
8863 P11	1.72±0.03	1.40±0.04	12.72±0.13
9015 P10	1.59±0.03	1.29±0.03	13.61±0.15
9069 [S III]	4.74±0.07	3.58±0.07	44.31±0.25
$C(H\beta)$		0.190±0.018	
EW_{abs} (Å)		1.3±0.2	
$F(H\beta)$ (10^{-14} erg s $^{-1}$ cm $^{-2}$)		4.3±0.2	

Table 5. Emission Line Fluxes and Equivalent Widths in the Integrated Spectrum of the H II Region

Line	$F(\lambda)^a$	$100 \times F(\lambda)/F(\text{H}\beta)$	$I(\lambda)^a$	$100 \times I(\lambda)/I(\text{H}\beta)$	$EW(\lambda)^b$
3727 [O II]	228.1± 7.1	21.87±0.68	468.0±14.9	25.82±0.82	23.95±0.45
3798 H10	49.1± 4.4	4.71±0.42	114.4±12.1	6.31±0.67	6.12±0.40
3835 H9	60.4± 6.3	5.79±0.60	138.1±16.3	7.62±0.90	6.67±0.62
3868 [Ne III]	218.9±10.2	20.99±0.98	438.4±20.7	24.19±1.14	24.21±1.10
3889 He I+H8	175.8±13.4	16.86±1.28	365.8±28.8	20.18±1.59	21.73±1.20
3968 [Ne III]+H7	225.0± 3.8	21.57±0.36	458.4±10.3	25.29±0.57	26.58±0.20
4026 He I	15.3± 1.3	1.47±0.12	29.9± 2.4	1.65±0.13	1.73±0.13
4101 Hδ	268.3± 4.4	25.72±0.42	532.9±11.4	29.40±0.63	30.79±0.24
4340 Hγ	462.8± 7.7	44.37±0.74	870.9±15.4	48.05±0.85	79.26±0.57
4363 [O III]	102.4± 3.7	9.82±0.35	190.0± 6.9	10.48±0.38	19.32±0.51
4471 He I	35.8± 1.5	3.43±0.14	65.3± 2.7	3.60±0.15	6.57±0.24
4686 He II	36.9± 1.8	3.54±0.17	65.4± 3.3	3.61±0.18	6.70±0.26
4740 [Ar IV]	9.3± 1.1	0.89±0.11	16.3± 2.0	0.90±0.11	1.76±0.24
4861 Hβ	1043.0±15.3	100.00±1.47	1812.5±27.0	100.00±1.49	213.40±0.61
4921 He I	12.0± 1.6	1.15±0.15	20.5± 2.7	1.13±0.15	2.58±0.41
4959 [O III]	1078.0±15.6	103.36±1.50	1842.0±26.8	101.63±1.48	204.80±0.27
5007 [O III]	3214.0±46.4	308.15±4.45	5458.5±79.4	301.16±4.38	576.20±0.34
5876 He I	115.9± 1.8	11.11±0.17	178.2± 2.9	9.83±0.16	27.80±0.16
6300 [O I]	8.6± 0.6	0.82±0.06	12.5± 0.9	0.69±0.05	2.36±0.15
6312 [S III]	6.6± 0.5	0.63±0.05	9.6± 0.9	0.53±0.05	1.69±0.12
6563 Hα	3447.9±49.8	330.58±4.77	4972.8±78.5	274.36±4.33	689.40±0.30
6583 [N II]	12.4± 0.5	1.19±0.05	17.9± 0.7	0.99±0.04	2.48±0.09
6678 He I	31.8± 0.7	3.05±0.07	45.5± 1.1	2.51±0.06	7.46±0.15
6717 [S II]	26.8± 0.6	2.57±0.06	38.1± 0.9	2.10±0.05	6.38±0.14
6731 [S II]	21.8± 0.7	2.09±0.07	30.8± 1.1	1.70±0.06	5.22±0.16
7065 He I	49.1± 1.0	4.71±0.10	68.0± 1.6	3.75±0.09	18.59±0.28
7136 [Ar III]	21.1± 0.8	2.02±0.08	29.0± 1.3	1.60±0.07	7.62±0.29
7281 He I	7.6± 0.7	0.73±0.07	10.3± 0.9	0.57±0.05	2.81±0.29
$C(\text{H}\beta)$			0.240±0.019		
EW_{abs}^b			0.9±0.4		

^aIn units 10^{-16} erg s⁻¹ cm⁻².

^bIn Å.